

Confined vortex breakdown generated by a rotating cone

By J. C. F. PEREIRA AND J. M. M. SOUSA

Instituto Superior Técnico/Technical University of Lisbon,
Mechanical Engineering Department, Av. Rovisco Pais, 1096 Lisbon Codex, Portugal
e-mail: msousa@alfa.ist.utl.pt

(Received 20 January 1997 and in revised form 20 November 1998)

Confined vortex breakdown generated by a rotating cone within a closed cylindrical container has been studied both by numerical simulation and by experimental techniques. A comprehensive investigation of the various flow regimes has been carried out by flow visualization. From laser–Doppler measurements of the entire flow field (three velocity components) detailed maps of the time-averaged flow structures for single and double breakdown have been constructed. Three-dimensional time-dependent simulations of steady and unsteady breakdown have been performed. Steady numerical and experimental flow fields obtained at Reynolds number 2200 for a gap ratio of 2 show notable agreement. At critical Reynolds numbers of approximately 3095, for a gap ratio of 2, and 2435, for a gap ratio of 3, the flow was observed becoming unsteady. The periodic behaviour exhibited by the unsteady flow suggested the occurrence of a supercritical Hopf bifurcation. This conjecture was confirmed by the evolution of the oscillation amplitude as a function of criticality, measured for a gap ratio of 3. The dynamical behaviour of unsteady vortex breakdown structures is depicted by numerical simulation of two distinct oscillatory regimes, at Reynolds numbers 2700 and 3100. A thorough analysis of the numerical results has shown that whereas the former regime is characterized by the steady oscillation of closely axisymmetric breakdowns, the latter displays precession of breakdown structures about the central axis. Additionally, it was observed that the mode bringing about the Hopf bifurcation is non-axisymmetric, with azimuthal periodicity of $\pi/2$ radians. From examination of measured velocity power spectra at higher Reynolds numbers, a transition scenario was also deduced. In the present case, the Ruelle–Takens–Newhouse theorem has been shown to apply.

1. Introduction

The great practical significance attributed to confined vortex flows proceeds from the widespread application of swirling flow in industrial processes and devices (see e.g. Escudier 1987). Throughout recent years we have learned to make advantageous use of most of the characteristics exhibited by sufficiently intense vortex flows, such as the large regions of recirculating flow, which are used for flame stabilization (Syred & Beér 1974), and the strongly dissipative nature, which finds application in vortex valves (Lawley & Price 1972). However, some of the features of vortex flows have proved to be pernicious in a number of situations as well. Induced vibrations and discrete-frequency noise have also been identified in various flow machinery, as a consequence of particular changes in the structure of the core of the swirling flow. Perhaps the most interesting transformation occurring in vortex flows is that termed ‘vortex breakdown’. This phenomenon, first observed by Peckham & Atkinson (1957) in the tip vortices

of a delta wing, has been the theme of much work with the aim of providing a better understanding of the underlying physical mechanisms, as demonstrated by several reviews (Hall 1972; Leibovich 1978, 1984; Escudier 1988). The continuing interest in the subject is mainly a result of the large variety of forms that have been recognized as a manifestation of the phenomenon (Sarpkaya 1971*a,b*; Faler & Leibovich 1977). Such diversity of characteristics has hampered efforts to establish a satisfactorily general interpretation of its fundamental nature and, consequently, the controversy persists.

Vortex breakdown has been defined as an abrupt change in the character of vortex cores (Benjamin 1962). In more recent years the concept has evolved and it has incorporated the observation that this change is often characterized by the formation of internal stagnation points and regions of reversed flow. The theoretical investigation of vortex breakdown was initially based on wave-motion theories (Squire 1960; Benjamin 1962, 1967). Similar approaches have also been pursued by Randall & Leibovich (1973), who hypothesized a model based on a theory of weakly nonlinear waves propagating on critical flows, and by Escudier & Keller (1983), who extended Benjamin's conjugate-state transition ideas by formulating the hypothesis of a two-stage transition. Recently, Leibovich & Kribus (1990) have also followed the concepts introduced by Benjamin and found solitons in inviscid vortex flows that may be also the origin of some vortex breakdown structures. Vortex instability was also conjectured for the explanation of breakdown, first by Jones (1960), and later by Lessen, Singh & Paillet (1974), Garg & Leibovich (1979) and Leibovich & Stewartson (1983), to name a few. However, as pointed out by Escudier (1988), there is not much evidence from experimental investigations to support the view that instability plays a major role in vortex breakdown.

The awareness of the inherent difficulties in finding a complete theory of vortex breakdown has led to a substantial number of experimental studies. By imparting swirl to the fluid in an upstream guidevane arrangement, radially confined and highly axisymmetrical vortices have been generated in tubes by Lambourne & Bryer (1961), Harvey (1962), Cassidy & Falvey (1970), Sarpkaya (1971*a,b*, 1974), Faler & Leibovich (1977, 1978), Bornstein & Escudier (1984), Escudier & Keller (1985) and many others. Escudier and his co-workers have nevertheless preferred the slit-tube arrangement in their investigations (Escudier, Bornstein & Zehnder 1980; Escudier, Bornstein & Maxworthy 1982; Escudier & Zehnder 1982; Escudier 1983), claiming that a thinner vortex core could be produced by the use of this alternative flow system. Another flow configuration that has been employed in the study of vortex breakdown is the closed cylindrical container, where the fluid motion is established by a rotating element located at one end of the cylinder. Several researchers have adopted this device in their experimental studies since it can provide virtually perfect axisymmetric flows under highly controlled conditions. Thus, Vogel (1968) and Escudier (1984) have performed visualization experiments, which provided significant insight into the morphology of confined vortex breakdown generated inside cylindrical containers. Moreover, the detailed laser-Doppler measurements of Ronnenberg (1977) have confirmed Vogel's conclusions, but quantitative descriptions of the entire flow structures in this kind of confined breakdown are scarce.

The emergence of new experimental techniques, such as the combination of particle tracking velocimetry and volume scanning, have recently provided detailed measurements of bubble- and spiral-type structures in unsteady and non-axisymmetric vortex breakdown (Brücker & Althaus 1992, 1995; Brücker 1993). Using the guidevane apparatus, these authors have identified a tilted vortex-ring-like structure precessing about the longitudinal axis, in close agreement with previous observations by Sarpkaya.

During the last decade, numerical simulations of vortex breakdown have received special attention as a direct consequence of the advent of more powerful computing facilities. Lugt & Haussling (1982) performed the first numerical study of swirling flow confined to a cylindrical container that could reproduce the occurrence of breakdown. Since then, other solutions displaying steady vortex breakdown have been obtained for the same geometry by Lugt & Abboud (1987), Daube & Sørensen (1989) and Lopez (1990). The unsteadiness of the phenomenon was subsequently investigated by Lopez & Perry (1992) and Sørensen & Christensen (1995), using nonlinear dynamical systems theory to interpret the mutations observed in the flow kinematics. These excellent studies were, unfortunately, limited by the restrictive premise of axisymmetric flow. Few three-dimensional time-dependent simulations of vortex breakdown have been reported in the literature. The work of Liu & Menne (1989), Spall, Gatski & Ash (1990) and Breuer & Hänel (1993) are notable exceptions, but these authors considered synthetic initial conditions (e.g. a Burgers vortex) and their definition of boundary conditions was somewhat arbitrary. As a consequence, the validation of their results against experiments can only be made on qualitative grounds.

In this paper, the swirling flow driven by a rotating cone within a closed cylindrical container is investigated employing numerical and experimental techniques. The main idea behind the use of a conical driver instead of the classical flat rotor was that, from a topological point of view, the apex of a cone would provide a well-defined nodal point for the central streamline impinging upon the rotor wall. Thus, the present geometry is a simple variant of that employed by Vogel (1968) and Escudier (1984). Regardless of the expected similarities between the aforementioned investigations and the present one, it will be shown that this study extends our understanding of these flows in a substantial manner. This objective has been achieved by emphasizing the analysis of formally three-dimensional time-dependent regimes.

It was observed that, for some combinations of gap ratio (see figure 1*b*) and Reynolds numbers, the confined vortex undergoes breakdown. The various flow regimes have been experimentally identified and characterized. A systematic comparison between detailed laser-Doppler measurements of the entire flow field and results of a numerical simulation was performed for a steady regime exhibiting vortex breakdown. The full three-dimensional time-dependent Navier-Stokes equations, formulated in curvilinear coordinates to account for the complexity of the flow geometry, have been solved. Hence, it was possible to reveal striking features of the morphology and dynamics of oscillatory vortex breakdown confined to a closed cylindrical vessel. The analysis of experimentally obtained power spectra for unsteady regimes has further allowed a route to turbulence in the present flow to be postulated.

The paper is divided into five sections. In §2, the experimental techniques are described. This includes a description of both visualization and measuring procedures. The theoretical equations and the numerical methods used are presented in §3. Section 4 comprises the presentation and discussion of the results, followed by a brief summary of the main findings in §5.

2. Experimental arrangement and procedure

2.1. Test section and instrumentation

The experimental setup is schematically depicted in figure 1(*a*) and the essential features of the test section are shown in detail in figure 1(*b*). The flow was confined to a Duran glass cylinder, geometrically characterized by the inner radius $R = 0.050$ m

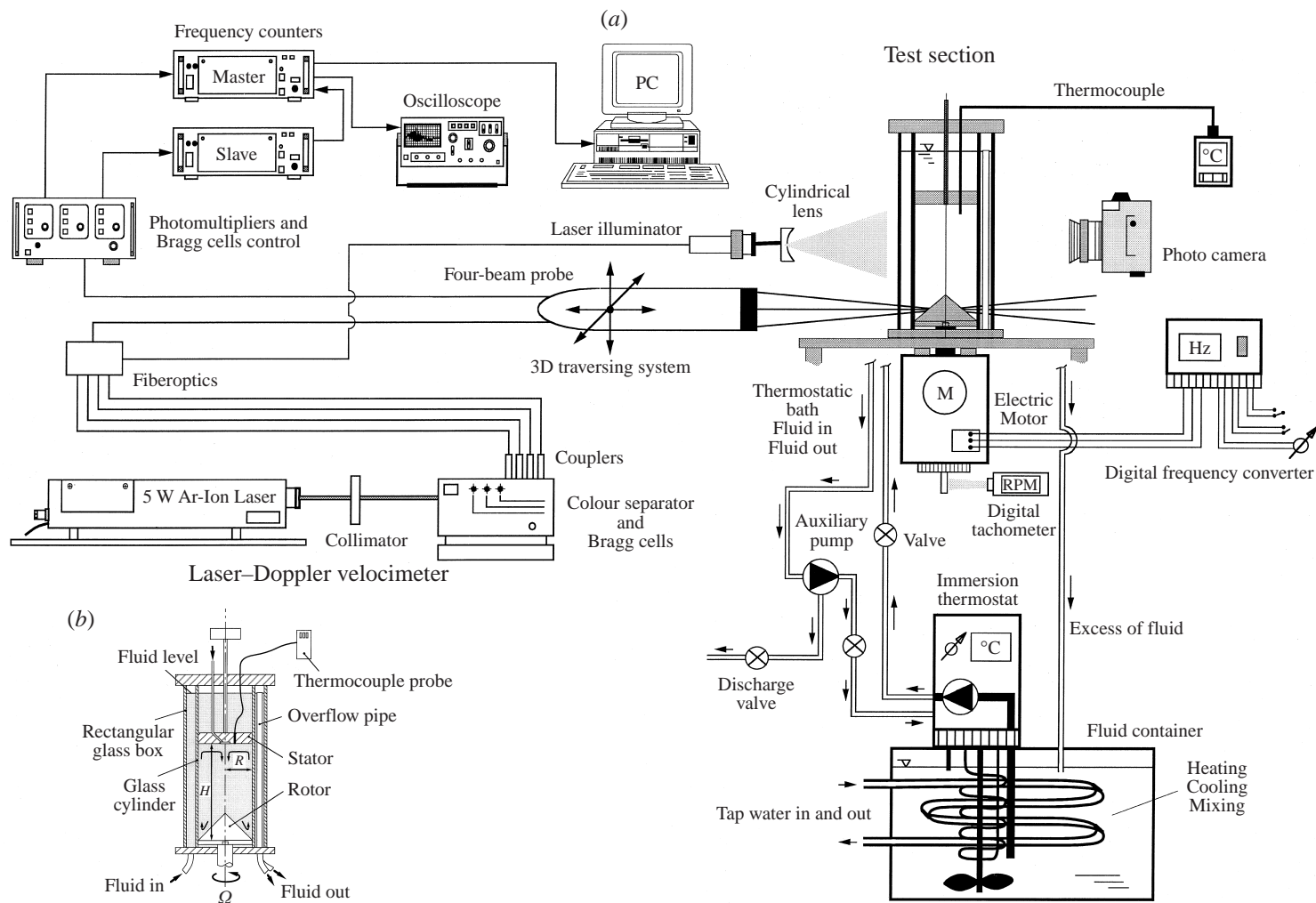


FIGURE 1. (a) Schematic diagram of the experimental setup; (b) test section.

Phase	Working fluid	Kinematic viscosity
Flow visualization	1/5 water+4/5 glycerine	$49.8 \times 10^{-6} \text{ m}^2 \text{ s}^{-1}$ @ 25 °C
Velocity measurements	Baby oil	$31.2 \times 10^{-6} \text{ m}^2 \text{ s}^{-1}$ @ 21 °C

TABLE 1. Working fluids used in the investigation.

and the height H , adjustable up to the maximum value of the gap ratio $H/R = 4$ by the use of a screw attached to the stator. The working fluid was set into motion by a rotating cone of height R (the rotor) that was driven by an electronically controlled motor. This allowed the spinning velocity of the rotor to be adjusted in a continuous range between 30 r.p.m. ($\Omega = 3 \text{ rad s}^{-1}$) and 1500 r.p.m. ($\Omega = 157 \text{ rad s}^{-1}$). A digital tachometer with a photocell was permanently active to ensure the accuracy of the velocity (± 0.1 r.p.m. in the range 30–1000 r.p.m. and ± 1 r.p.m. in the range 1000–1500 r.p.m.). Nevertheless, in order to guarantee stable operating conditions, the cylindrical container was also immersed in a thermostatically controlled bath, so that the fluid viscosity could be kept constant. This procedure was applied with the additional aim of matching the refractive index of the fluid with that of the glass walls. Thus, the fluid inside the cylinder was used in the bath as well, controlling the corresponding temperature to ± 0.1 °C with the use of Grant TD immersion thermostat and a copper coil in which cooling water was circulated. The fluid was pumped from the reservoir at the bottom to the test section at the top and then recirculated inside the (rectangular) glass box surrounding the cylinder. Although the fluid was usually returned to the reservoir by gravity, a secondary pump was used when larger flow rates were required. The fluid level in the test section was maintained constant merely by using an overflow pipe, its height determining the intended level as shown in figure 1(b). As the heat transfer between working and recirculating fluids was taking place through a 5 mm thick glass wall, a secondary control system was installed to prevent any generation of local temperature gradients. This system consisted of a type-K (compensated) thermocouple probe, inlaid in the stator wall during the measurements but still allowing exploration of the whole space between the walls and the rotor (fundamentally to avoid the presence of fluid stratification).

The selection of the working fluid was essentially determined by the requirement of applying a refractive index matching procedure during the course of the velocity measurements. This procedure minimized the problem of distortion of the optical paths through the curved surfaces in the liquid flow, so that reliable measurements close to the walls could be carried out (see e.g. Pereira 1989). Other requirements were imposed by specific physical properties of the fluid, with particular emphasis on an appropriate viscosity value and a chemically inert behaviour and, finally, with respect to flow visualization (demanding considerable amounts of fluid), by its cost. For these reasons, two different fluids were employed, depending upon the phase of the present investigations, as shown in table 1. The viscosities were measured using a digital viscometer Brookfield (model DV-II) and those values were often confirmed during the experiments.

2.2. Flow visualization

Flow visualization was used to portray the salient features of steady and unsteady regimes exhibited by the flow problem under investigation, before embarking on

detailed quantitative measurements. In addition, this enabled us to establish a 'road map', as will be shown in §4, guiding later stages of this study.

Common to the flow visualization techniques employed to achieve our objective was laser light sheet illumination. A 5 W Ar-ion laser was used as light source, together with a fibre-optic illuminator to facilitate the placing of the light sheet on the flow centreline. Laser beam expansion, to generate the light sheet (about 1.5 mm thick), was accomplished with the help of a cylindrical lens. In some cases, to guarantee a homogeneous illumination of the whole area of interest, an adjustable mirror was required. Still photographs were taken at right angles to the sheet of light.

The most natural way of rendering flow motion visible is probably the one that makes use of the light scattered by small particles. In the present case, particles had to be added to the flowing fluid, hence some care was taken in order to make sure that the motion of those particles closely approximated that of the fluid. Spherical polystyrene particles (1–10 μm in diameter) were selected, displaying an adequate response to rapid changes of the flow field and a quasi-neutral buoyant behaviour. This procedure was broadly used to characterize steady regimes, although a few instantaneous pictures of unsteady regimes have been obtained as well. However, the interpretation of such observations in time-dependent flows is severely complicated by the fact that, unlike steady flows, streamlines, streaklines and pathlines do not generally coincide, as discussed by Merzkirch (1974). Aware of this pitfall, we did not make extensive use of this technique to interpret the unsteady fluid motion. The usage of an ultraspeed film (3200 ASA) allowed us to obtain well-contrasted black/white photographs for fairly reduced exposure times (typically 1/8 to 1/2 s).

The second flow visualization technique employed in the present investigations was the injection of fluorescent dye. Dilute solutions of solid crystals of Fluorescein and Rhodamine-6G were prepared and carefully injected into the flow (with the aim of minimizing the inherent disturbance), generating thin threads of dye which became intensely bright when excited by the coherent light source. The anatomy of the flow was thereby unveiled, providing complementary observations of the flow structures. As a result of the strong fluorescence, ordinary daylight film (100 ASA) could be used to produce colour photographs.

2.3. Velocity measurements

Laser-Doppler velocimetry (LDV) was extensively used during the quantitative phase of the experiments. It is an expeditious technique for the measurement of the velocity field associated with complex flows, having the substantial advantage of being non-intrusive. Many details of the fundamentals and the principal aspects associated with the application of LDV to fluid flow problems can be found in the literature (see e.g. Durst, Melling & Whitelaw 1981; Adrian 1983).

The measurements were taken with a two-component LDV system from TSI Inc. A 3 W (nominal) Ar-ion laser was employed for the velocimeter, which was operated in the dual-beam (two green and two blue) backward-scatter mode. In order to provide sensitivity to the flow direction, the system included an acousto-optic modulator, which was set to generate a shift frequency of 200 kHz. The velocimeter transfer constants were 5.315 (m s^{-1})/MHz and 5.042 (m s^{-1})/MHz, respectively for green and blue beams. The backward-scatter light (green and blue) was collected through transmitting and receiving lenses, focused into a multimode receiving fibre, collimated with a double-input coupler and finally passed into a colour separator so that the scattered light coming from each pair of laser beams could be isolated. Two photomultipliers translated this input into analog signals which were monitored

by a two-channel oscilloscope, filtered and processed using two frequency counters (TSI 1990C) interfaced with a digital computer. Velocity values were evaluated by ensemble averaging, calculated from 5000 samples, using TSI FIND Software. The same software was used to control a three-dimensional ISEL traversing system where a fibre-optic probe incorporating both transmitting and receiving optics was mounted. In order to map the three-dimensional velocity field, two traverses through meridional planes of the cylinder had to be carried out for each station along the axial direction. During the first one, both axial and radial components were measured, and during the second the circumferential component was measured. Figure 1(a) shows a schematic diagram of this apparatus.

The errors incurred in the measurement of velocities are usually classified in two major categories: systematic and random (or statistical). Within the first category, non-turbulent Doppler broadening errors due to gradients of mean velocity across the measuring volume and sampling bias are, in general, the prevalent sources of uncertainty. However, as this affects essentially the variance of the velocity fluctuations (see e.g. Durst *et al.* 1981), its effect on mean velocities was negligibly small. With respect to the latter, it was only possible to minimize its consequences by using high seed rates compared to the fundamental velocity fluctuation rates, as suggested for example by Dimotakis (1976) and Erdmann, Lehmann & Tropea (1986). However, Yanta & Smith (1973) have proposed a theory that provides us with estimates for the statistical errors in this category. According to their analysis, the number of individual samples used to form the averages during the course of the present velocity measurements allowed us to keep the random errors below 2%, for a 95% confidence level. Thus, the various sources of errors suggested an uncertainty for the time-averaged velocities of less than 4%.

The *a posteriori* analysis of the measured time series also made possible the investigation of the spectral content of particular flow regimes, by calculating power spectra and corresponding probability-density functions. It is well known that, in a power spectrum, the frequency resolution is $1/T$ (if no averaging is employed to reduce statistical noise), where T is the 'length' of the data record; the maximum frequency that can be accounted for is the Nyquist frequency, $\omega_N = \omega_S/2$, ω_S representing the sampling frequency (see Bendat & Piersol 1971). In order to clearly identify the various dynamical regimes displayed by the flow under investigation, it is desirable to retain high spectral resolution and, simultaneously, to cover a wide spectral band, demanding $N = \omega_S T \gg 1$. The results to be presented in §4 were typically obtained for $N = 2^{13}$ samples. It should be mentioned that the value of ω_S varied from case to case, determined by the flow conditions, and the presence of spurious components in the power spectra ('aliasing') was avoided by comparing two equivalent measurements obtained with two different values of ω_S (typically related by a ratio of 10).

Aiming to minimize sampling errors and the presence of noise in the power spectra computed from frequency counters signals, we have followed the suggestions of Dimotakis (1976), Edwards & Jensen (1983) and Adrian & Yao (1987). Accordingly, the data rate values were always kept above 400 Hz. Further, although Erdmann *et al.* (1986) have demonstrated that bias errors can be more important in periodic flows, it was observed that the zones of the flow characterized by the highest amplitudes of periodic oscillation were also those where the time-averaged velocity was close to zero and the probability-density distributions were nearly bimodal, such that the bias of the negative velocities offset that of the positive velocities.

3. Numerical formulation

3.1. Governing equations

The mass and momentum conservation equations for the unsteady flow of an incompressible fluid can be written in vector form, independently of the coordinate system, as

$$\nabla \cdot (\rho \mathbf{v}) = 0, \quad (1)$$

$$\frac{\partial}{\partial t}(\rho \mathbf{v}) + \nabla \cdot (\rho \mathbf{v} \otimes \mathbf{v} - \boldsymbol{\tau}) = \mathbf{S}_F, \quad (2)$$

where the stress tensor $\boldsymbol{\tau}$ for a Newtonian fluid, from Stokes' hypothesis, is given by

$$\boldsymbol{\tau} = -(p + \frac{2}{3}\mu \nabla \cdot \mathbf{v})\mathbf{i} + \mu(\nabla \mathbf{v} + \nabla^t \mathbf{v}). \quad (3)$$

In the above equations ρ stands for the fluid density, μ for the dynamic viscosity, p for the pressure, \mathbf{v} for the velocity vector and \mathbf{i} for the unit tensor of second order. On the right-hand side of (2), the source term S_F accounts for the presence of body forces.

At this stage, in order to split the vectorial momentum equation (2) into scalar equations, the coordinate system must be selected. Out of the multiplicity of possible choices, we preferred a locally fixed coordinate system, employing the Cartesian velocity components, which has proved to produce a much simpler formulation of the equations, where all vector and tensor components are expressed with reference to the Cartesian base vectors. Additionally, the awkward emergence of curvature terms (involving the Christoffel symbol), which account for the spatial variation of the base vectors, is thereby avoided. Thus, there is no reason to establish the distinction between contravariant and covariant components, which allows us to drop the tensorial formalism in the use of subscripts and superscripts. Further, expressing the divergence operator in the strong conservation form, the governing equations (1)–(3) can finally be written as

$$\frac{\partial}{\partial x_m}(\rho v_i C^{im}) = 0, \quad (4)$$

$$\frac{\partial}{\partial t}(\rho v_i) + \frac{1}{g^{1/2}} \frac{\partial}{\partial x_m} [(\rho v_i v_j - \tau_{ij}) C^{jm}] = S_{F_i}, \quad (5)$$

where

$$\tau_{ij} = -(p + \frac{2}{3}\mu \nabla \cdot \mathbf{v})\delta_{ij} + \frac{\mu}{g^{1/2}} \left(\frac{\partial v_i}{\partial x_m} C^{mk} \delta_{kj} + \frac{\partial v_j}{\partial x_m} C^{mk} \delta_{ki} \right), \quad (6)$$

$$C^{im} \equiv C_m^i = g^{1/2} \frac{\partial y^i}{\partial x_m}. \quad (7)$$

In equations (4)–(7), the symbols $\delta_{im} \equiv \delta^{im}$ denote Kronecker deltas, v_i indicates the Cartesian velocity component along direction i and g stands for the metric tensor, $g^{1/2}$ corresponding to the Jacobian of the coordinate transformation $y^i = y^i(x_m)$ between the curvilinear non-orthogonal coordinate system (x_1, x_2, x_3) and the Cartesian coordinate system (y^1, y^2, y^3) .

3.2. Discretization procedure and method of solution

The numerical approach using the finite-volume method is employed to discretize the governing equations (4)–(7) on a structured, non-orthogonal, non-staggered grid

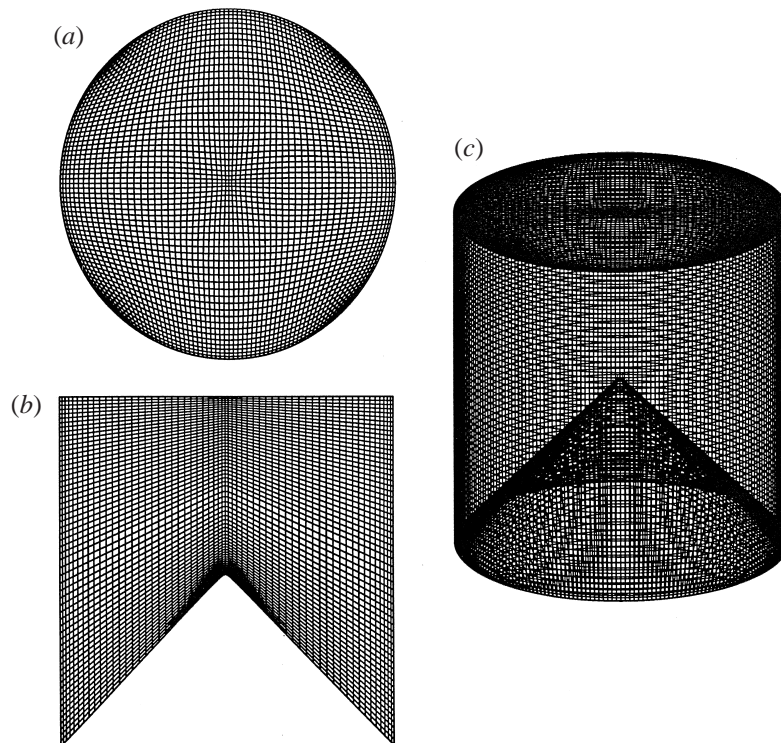


FIGURE 2. Example of the computational mesh: (a) top view; (b) meridional plane; (c) three-dimensional view.

system. The physical domain is discretized in control volumes (CV), defined by the coordinates of the eight vertices (grid nodes) of generally distorted cubes. A hybrid elliptic-algebraic procedure (see e.g. Thompson, Warsi & Mastin 1985) has been adopted for the definition of those cubes or, in other words, for the generation of the numerical mesh. An example of fine discretization ($61 \times 61 \times 61$ grid nodes) is illustrated in figure 2, for $H/R = 2$.

The discretization procedure can be briefly described as follows. Equation (5) is integrated in space, over each CV of the computational domain and in time, over a time interval Δt . The Crank–Nicholson time-stepping method is used to advance diffusion terms in time, while the second-order Adams–Bashforth method is applied to convection terms, rendering a fully second-order accurate time integration scheme (see e.g. Roache 1976). The implicit calculation of diffusion terms makes the present procedure semi-implicit. The time increment Δt is typically calculated from a CFL condition, where CFL stands for the Courant–Friedrichs–Lewy number. The remainder of the numerical method is, in essence, similar to that proposed by Coelho & Pereira (1993), the main difference being that, in the present method, both convection and diffusion terms are discretized using second-order-accurate central differences.

The pressure field is obtained from the solution of a pressure Poisson equation obtained by combining continuity and momentum equations, as shown e.g. by Pereira & Sousa (1993). However, as a non-staggered grid system was employed, the evaluation of the convective fluxes arising in the out-of-balance mass source term of the Poisson equation requires the interpolation of the velocity components at the faces of a CV .

In order to avoid decoupling between pressure and velocities, the practice proposed by Rhie & Chow (1983) and Kobayashi & Pereira (1991) is implemented as well.

The set of equations that we propose to solve is naturally subject to boundary conditions. Physically meaningful no-slip conditions, either for stationary or moving walls, are imposed on all boundaries confining the computational domain. The numerical treatment of such conditions is trivial, as the present formulation deals with the primitive variables of the flow. Finally, the numerical solution procedure entails solving a system of algebraic equations, which results from the discretization procedure. This is carried out by using the strongly implicit procedure of Stone (1968). Additional details regarding the numerical formulation are given by Sousa (1995).

4. Results and discussion

4.1. Flow regimes

The various flow regimes were experimentally observed by gradually increasing the angular speed, Ω , of the rotor (see figure 1*b*), initially at rest. As a result, a rotating boundary layer develops over the slanted surface of the rotor, starting the radial motion of the fluid, which moves away from the cylinder axis in spiralling trajectories. Owing to the presence of the cylinder walls, the fluid is forced to move upwards. This gives rise to the formation of a new boundary layer over the vertical solid surface, but the spiralling motion is maintained. Except for viscous losses, the fluid conserves its angular momentum while moving towards the top wall (stator), which is reached eventually. Then, a three-dimensional boundary layer is again established, retarding the fluid in the vicinity of the wall. To preserve the balance between radial pressure gradient and centrifugal forces, this deceleration further induces a reduction in the radius of the fluid trajectories in this region, directing the fluid, once more, to the cylinder's axis. Thus, the convergence of rapidly rotating fluid paths to the centreline starts the creation of a concentrated vortex core. Finally, the flow is maintained by continuity, as the rotor draws the spiralling fluid down this central vortex, repeating the process by sending it, once again, outwards to the side walls.

Based on the above description, it seems natural to conclude that the velocity field corresponding to the flow inside the cylinder is driven by an axial component, limited in its growth due to geometrical restraints (the rotor and the stator), and by a swirl component, always increasing as Ω increases. As a consequence of the continuous increase in swirl, vortex breakdown is expected to occur (Hall 1972). However, in the present case, the appearance of the phenomenon with increasing Ω has been shown to be a smooth process, in agreement with the bifurcation analysis carried out by Tsitverblit (1993). This behaviour is sequentially illustrated in figures 3 and 4, obtained by flow visualization (laser light sheet and particles) for increasing values of Ω . Thus, as the occurrence of breakdown does not present the abruptness of a critical event, it is necessary to adopt a specific criterion for the identification of its appearance and disappearance. The presence of a stagnation point in the central axis, invariably heralding the formation of a recirculation bubble, seemed to be the most sensible criterion for the appearance of a steady breakdown. Correspondingly, the absence of stagnation points in the central axis provided evidence of the disappearance of steady vortex breakdown.

The photographs in figure 3 refer to $H/R = 2$, for several values of the Reynolds number $Re = \Omega R^2/\nu$. In figure 3(*a*), the flow is as described in the first paragraph of this Section ($Re = 1090$): the flow establishes a single large recirculation area, occupying the whole cylinder. However, figure 3(*b*) displays that, as Re increases to 1320, the fluid undergoes a sudden deceleration at the axis, near the top of the rotor, with

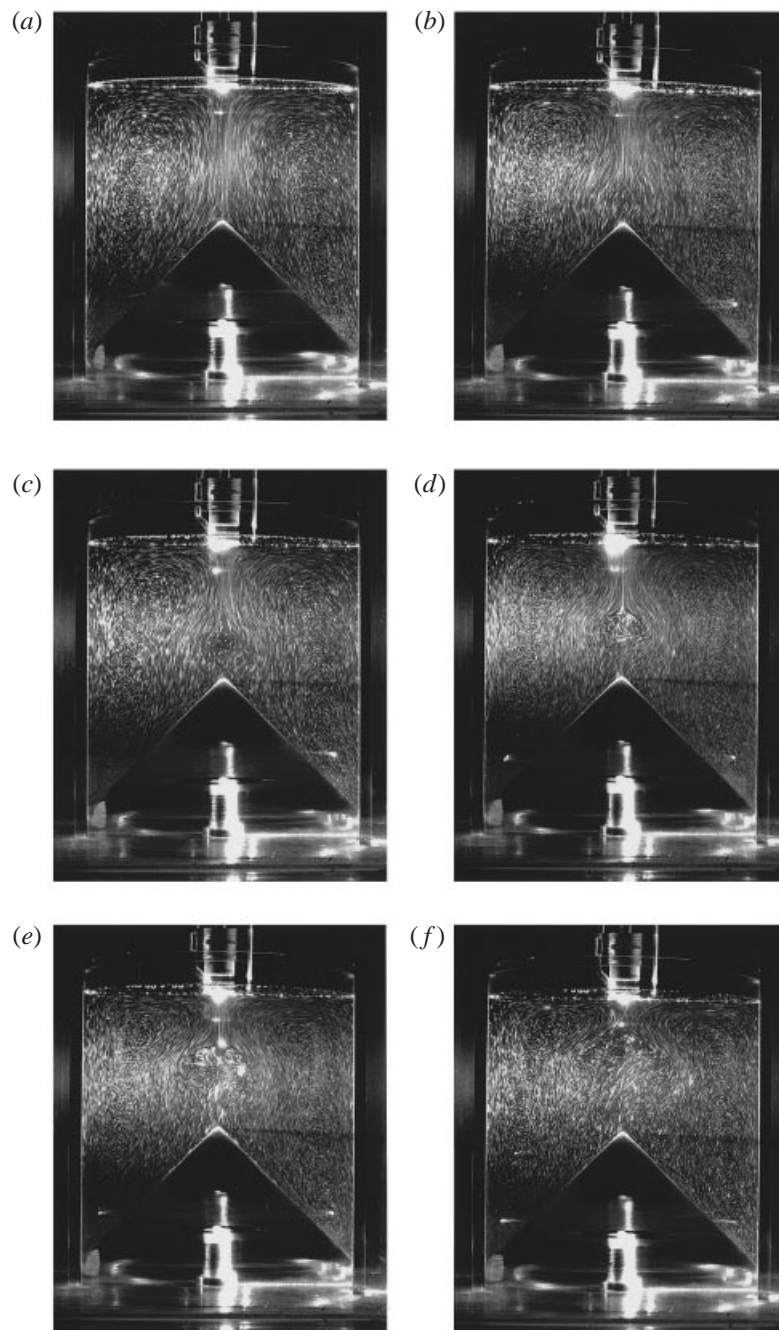


FIGURE 3. Flow visualization of changes in flow structure for $H/R = 2$: (a) $Re = 1090$; (b) $Re = 1320$; (c) $Re = 1395$; (d) $Re = 1555$; (e) $Re = 1880$; (f) $Re = 2560$.

the concomitant divergence of adjacent fluid trajectories (enlargement of the vortex core). Subsequent to the appearance of a stagnation point, this region of the flow gives rise to a small recirculation bubble, associated with the incipient formation of vortex breakdown. As Re is progressively increased to 1395, 1555, 1880 and 2570 (figures

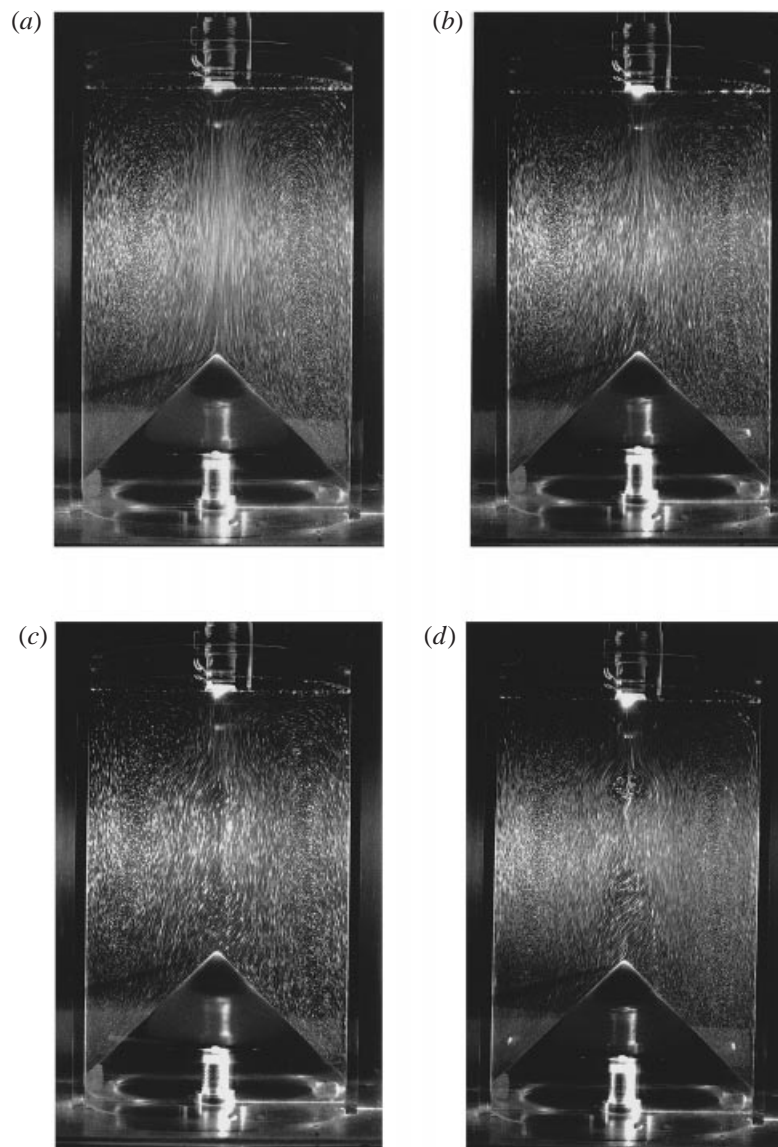


FIGURE 4(a-d). For caption see facing page.

3c–3f), the flow visualization shows the maturation of this bubble (clearly observed in figure 3d) and its upwards migration. During this process, the recirculation bubble, hereinafter referred as vortex breakdown, grows continuously in the radial direction. As a result, the breakdown bubble is seen to assume disproportionate dimensions, its boundaries, formerly well defined, becoming increasingly vague (figure 3f). These symptomatic characteristics indicate that the recirculating flow structure cannot exist anymore and, in fact, it was possible to witness its extinction at slightly higher values of Re .

An identical procedure was followed for $H/R = 3$. Thus, one can readily view that from figure 4(a) to figure 4(b) the swirl effects are emphasized, as shown by the divergence of fluid trajectories in the latter image, as described earlier for $H/R = 2$.

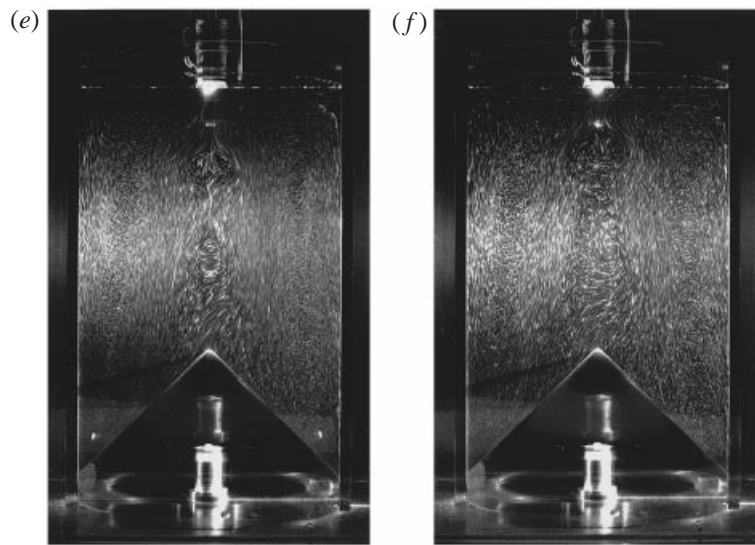


FIGURE 4. Flow Visualization of changes in flow structure for $H/R = 3$: (a) $Re = 1590$; (b) $Re = 2065$; (c) $Re = 2200$; (d) $Re = 2390$; (e) $Re = 2515$; (f) $Re = 2970$.

Still, it is not possible, at that stage ($Re = 2065$), to detect any stagnant fluid. Conversely, figure 4(c) exhibits the initial formation of a double breakdown ($Re = 2200$). The increase in angular speed gives rise to a primary bubble, located not very far from the top wall, and a secondary bubble, more stretched and less well defined, that settles underneath. One should note that the formation of both recirculation bubbles is nearly simultaneous, though careful observations allowed to conclude that the primary breakdown occurs slightly earlier than the secondary breakdown. At $Re = 2390$ (figure 4d) and 2515 (figure 4e), the bubbles are clearly established. The upward movement is, once again, clear, concurrently bringing the structures closer to each other. At higher values of Re , in this case well before the dissipation of the recirculation bubbles, the flow is observed to be notably time-dependent: we must stress that figure 4(f) is an instantaneous snapshot of a flow regime ($Re = 2970$) which is, actually, periodic. A very slight unsteadiness already exhibited at $Re = 2515$ is not perceptible in figure 4(f).

The above description constitutes only a brief, albeit comprehensive, excerpt of the extensive flow visualization study conducted during the course of the experiments, which allowed us to establish a 'stability diagram' for confined swirling flow generated by a rotating cone. The resemblance between the diagram depicted in figure 5 (present case) and a comparable representation for the case of a rotating disk, mapped by Escudier (1984), is, as one might suspect, readily apparent. The main discrepancy lies on the shift of the main curve (singly breakdown) to larger values of H/R and Re . Additionally, it can be seen that the area corresponding to double breakdown is, again for the present case, significantly reduced. A simple explanation for these differences can be found by recognizing that the space available at the central axis is smaller for the case of a rotating cone, therefore inhibiting the occurrence of vortex breakdown. This also explains why triple breakdown did not occur for any combination of the parameters H/R and Re , in clear contrast to the flow investigated by Escudier. There is a considerable uncertainty associated with the dashed line in the diagram, marking the border between steady and unsteady flow, since the start

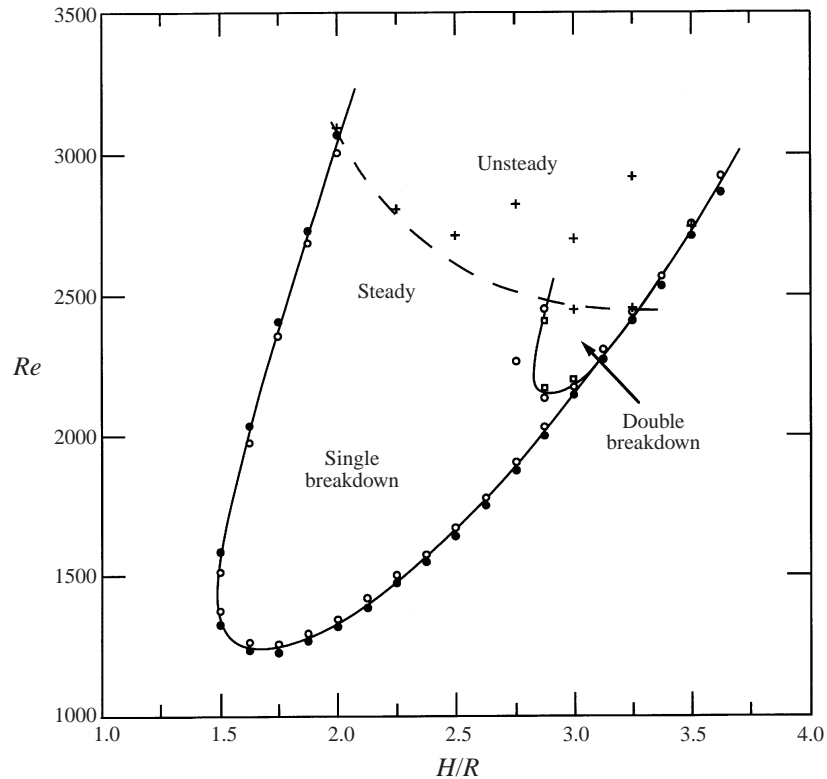


FIGURE 5. Stability boundaries for single and double breakdown, and the boundary between oscillatory and steady flow.

of time-dependent behaviour was very difficult to perceive. It was only detectable by the nearly undiscernible oscillation of the top stagnation point location. This matter will be addressed in detail later in §§4.3 and 4.4.

4.2. Steady breakdown

The application of LDV in conjunction with a refractive index matching technique made possible the accurate mapping of the complete three-dimensional velocity field in the presence of vortex breakdown. The extension of the measurements up to the walls, which could not be accomplished in similar experiments performed by Bornstein & Escudier (1984), was therefore achievable. Simultaneously, the procedure allowed the measurement of the radial velocity component, which is rarely reported for this type of flows (see e.g. Escudier 1988).

The velocity measurements were carried out for two regimes: $H/R = 2$ and $Re = 2200$; $H/R = 3$ and $Re = 2570$. These particular regimes were selected because both cases exhibit large and fundamentally steady breakdown bubbles (in fact, the second regime displays a slight unsteadiness). The projection of stream surfaces on one of the cylinder's meridional planes (hereinafter referred as 'streamlines') could be constructed from the measurements of the axial velocity component. Figures 6(a) and 6(b) portray the steady flow streamlines for each of the regimes, clearly showing the structure of the recirculation bubbles. As expected (see figure 5), single breakdown is obtained for $H/R = 2$, while double breakdown is observed for $H/R = 3$. In both cases, the flow is observed to be axisymmetric, within experimental accuracy. The

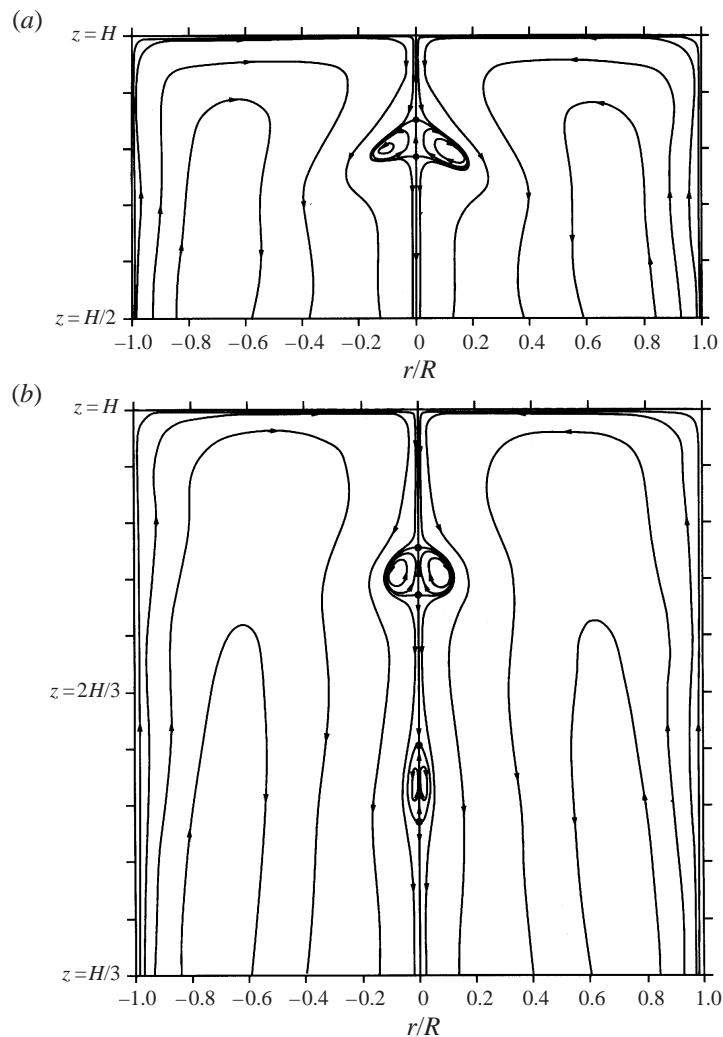


FIGURE 6. Streamline patterns constructed from axial velocity measurements: (a) $H/R = 2$ and $Re = 2200$; (b) $H/R = 3$ and $Re = 2570$.

large difference between the amount of fluid recirculated inside the bubbles and the main (external) flow rate is expressed as the ratio of the stream function maxima to the minima, for both of the above regimes: 1.6×10^{-3} for $H/R = 2$; 1.3×10^{-3} and 3.3×10^{-4} for $H/R = 3$, respectively corresponding to primary and secondary bubbles. Thus, one concludes that the fluid velocities inside the recirculation bubbles are much smaller than those occurring in the remainder of the flow, which may serve as an explanation for the small departure from axisymmetry displayed in figure 6(a). The numerical simulation of this flow regime would confirm the axisymmetry of steady vortex breakdown generated by a confined rotating cone, as will be seen in the next paragraphs. However, before the presentation of those results, we would like to examine another issue. The streamlines in figure 6 show that each breakdown bubble is bounded by a stagnation point. This could not be indisputably observed in the results of the flow visualization presented in the previous subsection, but the

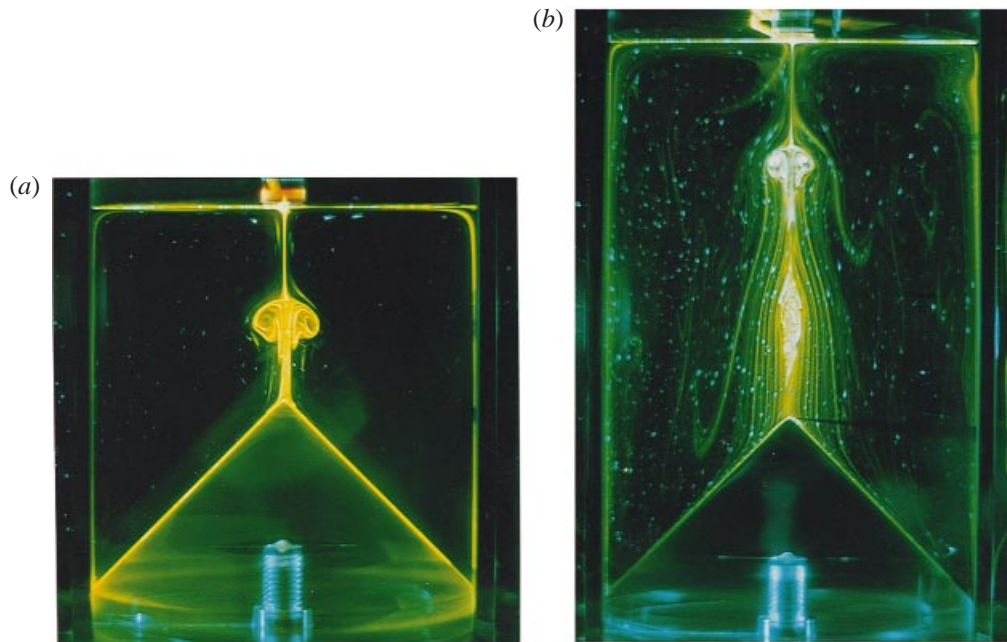


FIGURE 7. Visualization of vortex breakdown structures: (a) $H/R = 2$ and $Re = 1655$; (b) $H/R = 3$ and $Re = 2425$.

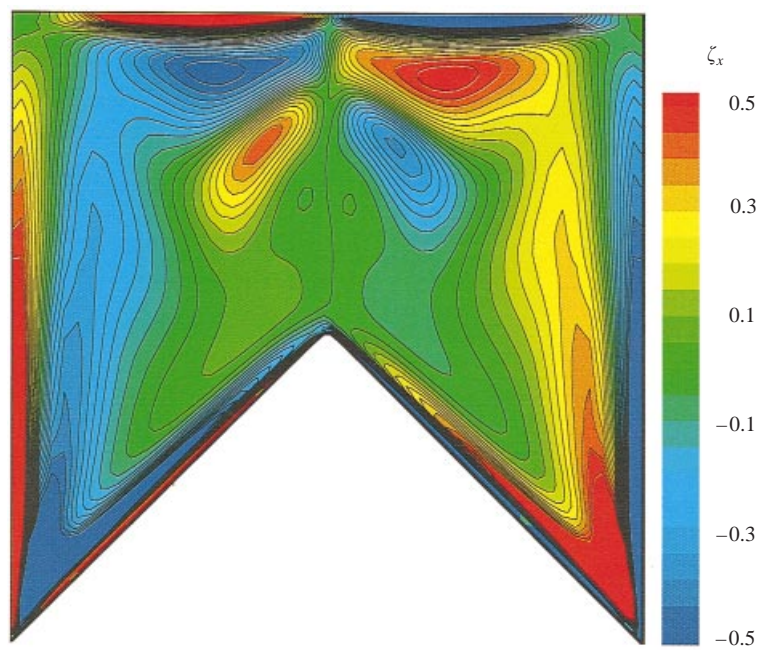


FIGURE 8. Contours of the Cartesian component of vorticity (normal to the meridional plane), calculated for $H/R = 2$ and $Re = 2200$.

use of fluorescent dye as tracer produced excellent photographs of the flow anatomy, revealing that all bubbles are ‘closed’ and similar in structure to those observed by Escudier (1984). Figure 7(a), displaying single breakdown for $H/R = 2$ and $Re = 1655$, and figure 7(b), depicting double breakdown for $H/R = 3$ and $Re = 2425$, show these results. An ‘open’ structure, such as that described by Bornstein & Escudier (1984) for a different flow geometry, was not to be found for the present steady regimes.

The three-dimensional numerical simulation of steady vortex breakdown was conducted for the regime characterized by $H/R = 2$ and $Re = 2200$ ($\Omega = 27.4 \text{ rad s}^{-1}$). The procedure adopted to perform the computations is described in detail in §3, but, in order to reduce the computational costs, the simulations were started from the first-order-accurate solution produced by the method of Coelho & Pereira (1993). The time step was selected in accordance to the condition $\max(CFL) \leq 0.4$, in order to comply with the stability constraints of the numerical method. Hence, the time-dependent simulation still required approximately 3500 time step to reach an asymptotically steady solution. During this process, the flow field was seen to evolve significantly from the initial condition to the final (second-order-accurate) result, as reported by Sousa (1995).

As we are dealing with a flow governed by vortical structures, we start the discussion of the computational results by presenting a vorticity map. Figure 8 shows the contours of the Cartesian component of the vorticity vector normal to the meridional plane, ζ_x (in this plane, the only difference between ζ_x and the azimuthal component is a change of sign through the axis). Taking advantage of the flow symmetry, we will refer to the left half of the plane only. The figure shows a region, adjacent to the sidewall, where ζ_x reaches the maximum positive value (red). It is followed by a larger intermediate zone, which is characterized by the maximum negative value (blue). In between these two regions, a narrow band of high vorticity gradients can be found. These features are consistent with the deceleration of the fluid in the vicinity of the wall, by viscous effects, giving rise to the development of a boundary layer. Most of the central area of the flow exhibits low gradients of ζ_x , as the inviscid effects dominate, basically corresponding to fluid in solid body rotation. The only exception to these smooth variations is a vortex ring of positive vorticity (naturally, only the cross-section is seen). Similar observations have been reported by Lopez (1990), providing a physical explanation for the occurrence of breakdown based on the ‘positive feedback mechanism’ (Brown & Lopez 1990). The vortex ring, initially formed as a result of the divergence of the axial flow while the fluid moves away from the top wall, induces a velocity reduction, in accordance with the Biot-Savart law. Consequently, a larger divergence of the streamlines is generated by mass conservation, which is, in turn, accompanied by the intensification of vorticity concentration. A stronger vortex ring induces a new deceleration of the axial flow, ultimately giving rise to the recirculation bubble. Significant amounts of vorticity can be observed to exist near the outer edges of the breakdown bubble, as experimentally observed by Brücker & Althaus (1995). Similar results have been also obtained in the numerical simulations performed by Spall *et al.* (1990) for a Burgers-type vortex, where the evaluation of the terms in equation for the rate of change of enstrophy was performed. Based on those results, they stated that, although the essential mechanisms in the origin of vortex breakdown are of inviscid character, a complete description of the phenomenon can only be achieved through the inclusion of viscous effects in the analysis. Additionally, these effects would be dominant in the region where the magnitude of the vortex-stretching term is smaller and, therefore, indispensable in obtaining the correct structure of the recirculation bubble.

The planar projected vectors picturing the organization of the flow field, corre-

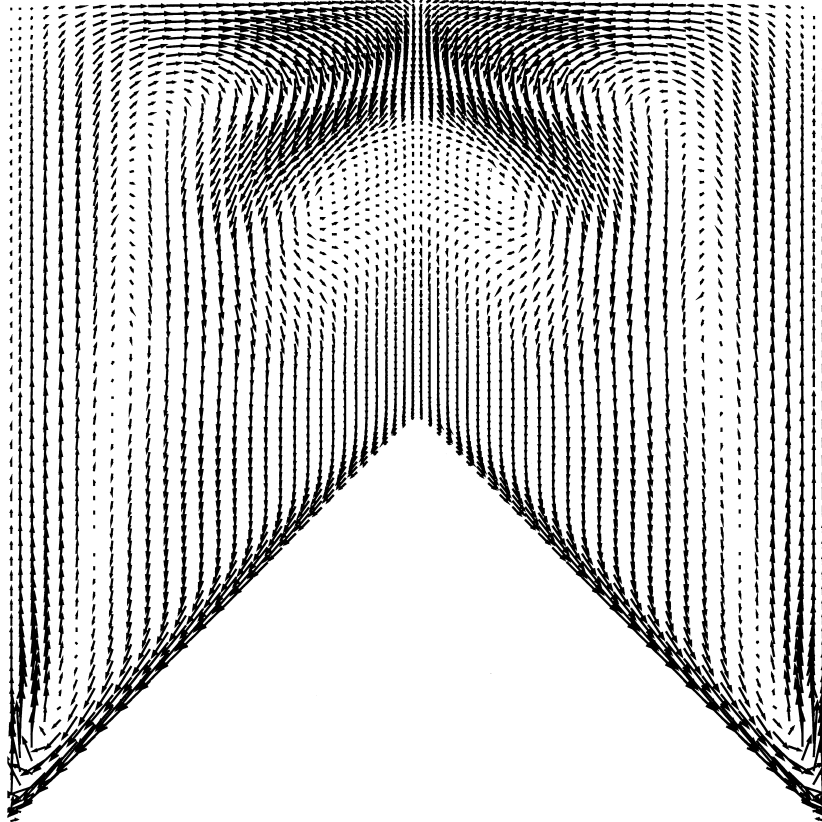


FIGURE 9. Planar projected velocity vectors at the meridional plane, calculated for $H/R = 2$ and $Re = 2200$.

sponding to the vorticity contours in figure 8, are shown in figure 9. The large dimensions of the bubble, which is unquestionably axisymmetric, and the strong velocity gradients along the upper region of its outer edge are the most salient features. A more elaborate examination of the flow details is presented in figures 10–12, which show a comparison between numerical predictions (lines) and LDV measurements (symbols), respectively for the axial, radial and circumferential velocity components. Formally speaking, the velocity components considered in those figures are the Cartesian components. However, for a meridional plane, these can be confused with their cylindrical counterparts (except for the change in sign occurring through the axis for radial and circumferential velocities). Although we are aware of these differences, a discussion referencing the latter components was preferred due to the cylindrical geometry of the present flow problem.

Figure 10(a–j) demonstrates the ability of the numerical method employed in the simulations to reproduce the minimum details of the flow field, concerning the axial velocity component (note that upward velocities have been plotted as negative, the origin of the z -axis is at the base of the cylinder and r is a radial coordinate). As discussed e.g. by Escudier *et al.* (1982), the axial velocity profiles exhibit a jet-like shape near the top wall, evolving to wake-like past the breakdown bubble. Still noteworthy is the insignificantly small value of the axial velocity within the bubble, covering a considerable area and influencing the region below. The agreement between

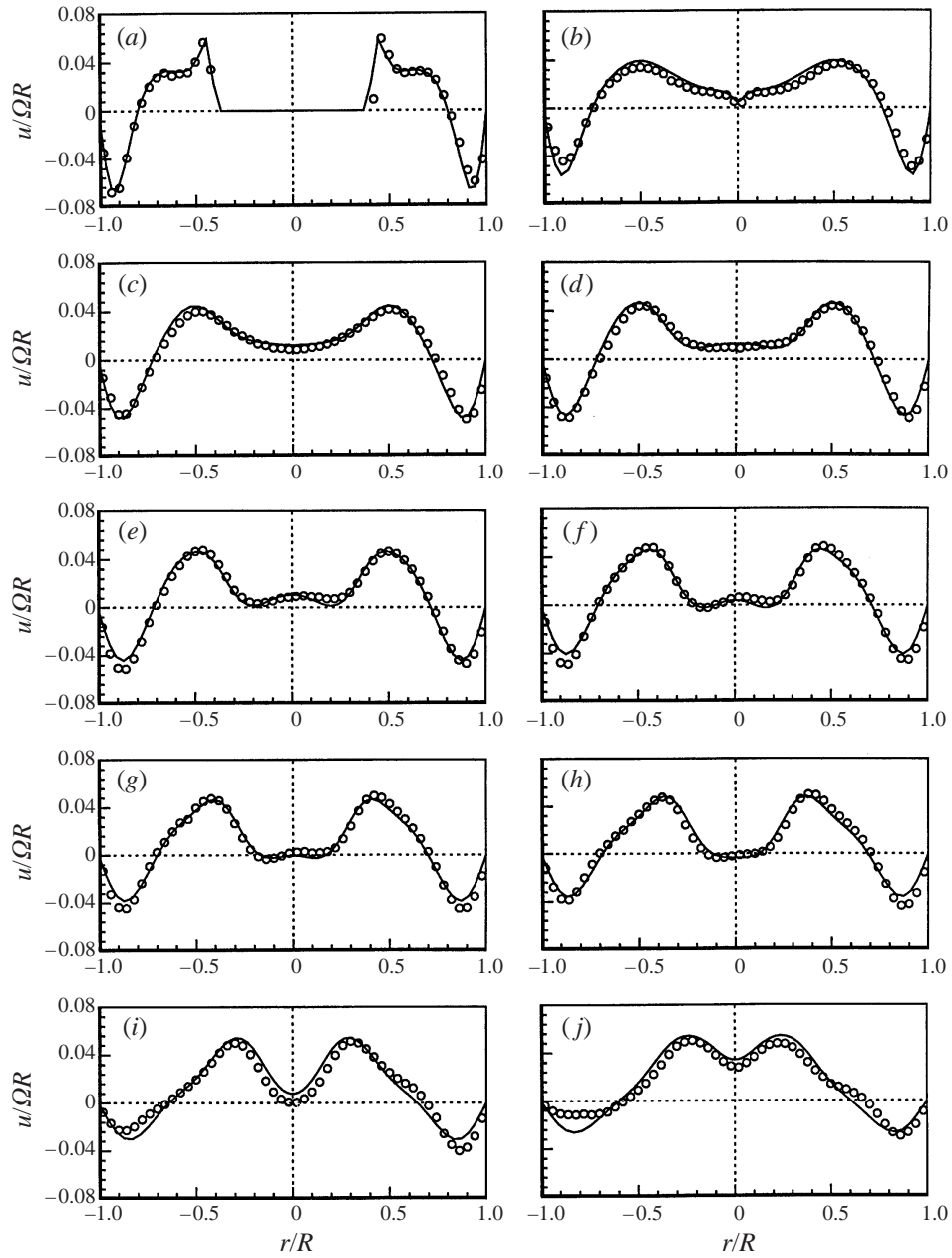


FIGURE 10. Measured (symbols) and computed (curve) axial velocity profiles for $H/R = 2$ and $Re = 2200$: (a) $z/R = 0.60$; (b) 1.00; (c) 1.20; (d) 1.30; (e) 1.40; (f) 1.50; (g) 1.55; (h) 1.60; (i) 1.70; (j) 1.80.

experiments and predictions is remarkable, excluding the two profiles near the stator where small discrepancies were caused by the abrupt velocity variations occurring in this zone (acceleration followed by stagnation). For this reason, an error of just 0.5 mm in the position of the measured velocity profile brings about significant differences in the magnitude of the axial velocity, which was confirmed by a sensitivity analysis of the location of the experimental profile with respect to its numerical counterpart.

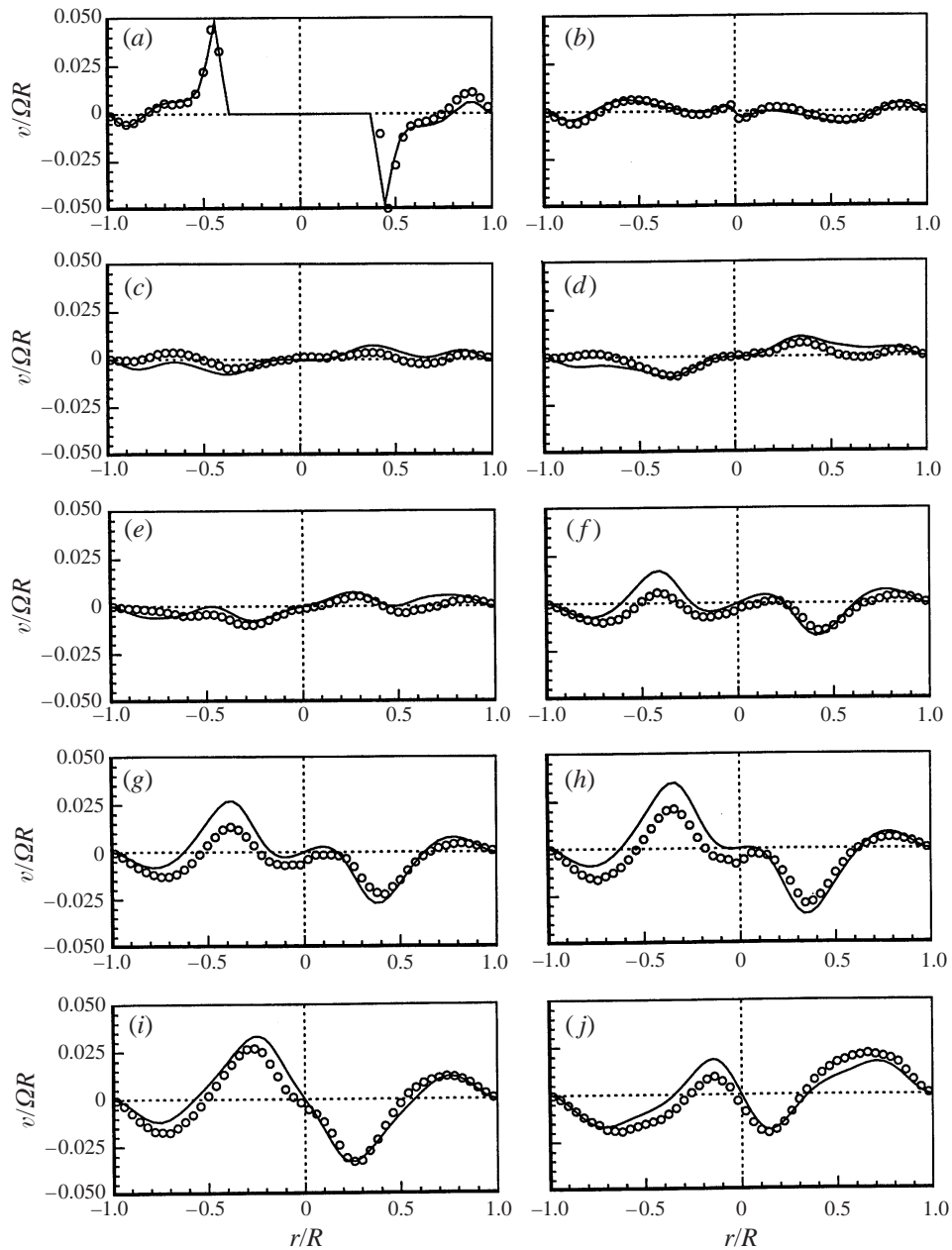


FIGURE 11. Measured and computed radial velocity profiles for $H/R = 2$ and $Re = 2200$: (a) $z/R = 0.60$; (b) 1.00; (c) 1.20; (d) 1.30; (e) 1.40; (f) 1.50; (g) 1.55; (h) 1.60; (i) 1.70; (j) 1.80.

The evolution of the profiles of the radial velocity component can be seen in figure 11(a–j). It is noticeable that, with the natural exception of the regions close to the top and bottom of the cylindrical container, the radial velocities only become significant as a consequence of the occurrence of breakdown. The recirculation bubble is, in addition, responsible for the flattening of the profiles below it. A new change in the shape of the radial velocity profiles takes place in the vicinity of the rotor, resulting from the development of the rotating boundary layer. Despite the substantial

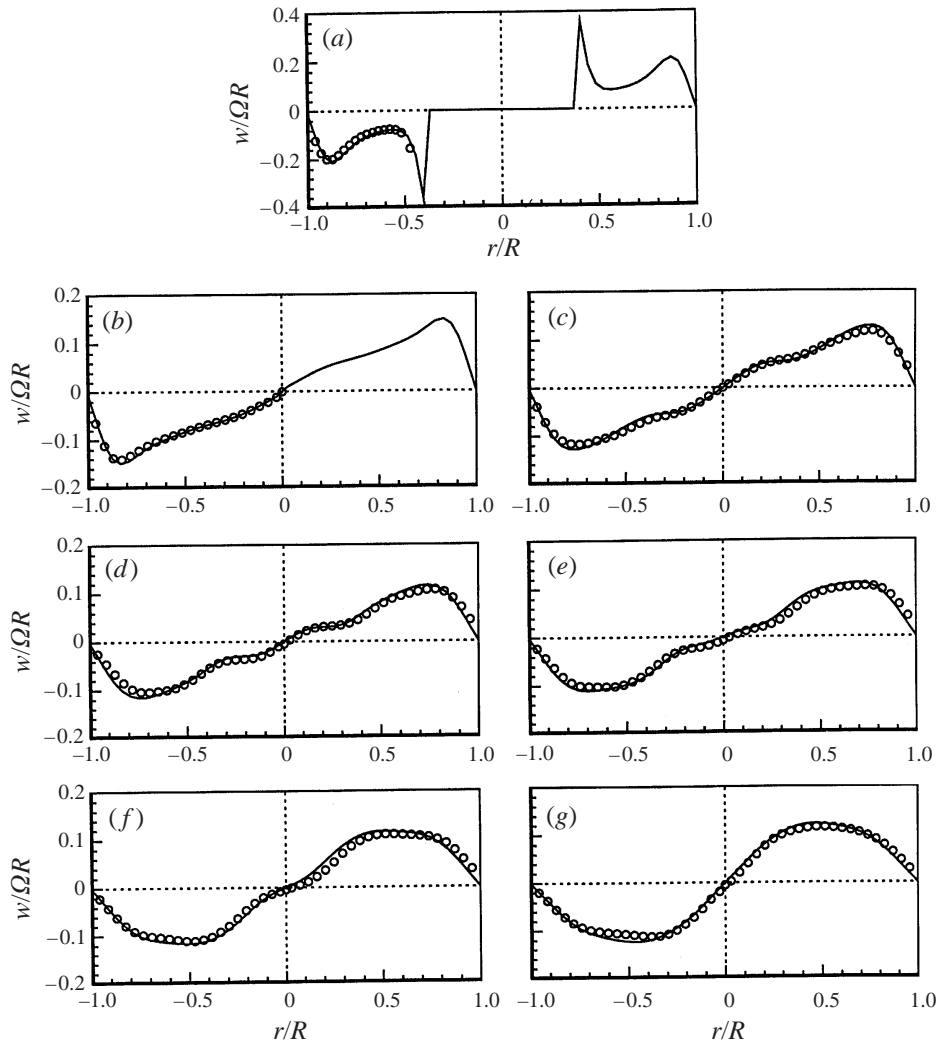


FIGURE 12. Measured and computed circumferential velocity profiles for $H/R = 2$ and $Re = 2200$: (a) $z/R = 0.60$; (b) 1.00; (c) 1.30; (d) 1.50; (e) 1.60; (f) 1.70; (g) 1.80.

variations observed in the magnitude of the radial velocity maxima at the various z -stations, the scale in all plots has been kept constant in order to show the disparity. The radial velocity values are generally low, which besides making the measurements more difficult, also makes this component very sensitive to small deviations from exact geometrical axisymmetry in the test section. Nevertheless, the results show that both experimental and numerical techniques showed, with reasonable accuracy, all the main characteristics of a radial velocity field for a flow dominated by vortex breakdown.

Finally, the profiles of the evolution of the circumferential velocity component throughout the cylinder are shown in figure 12(a-g). Note that the locations of these profiles do not exactly coincide with those presented for the other velocities. As the circumferential velocities show fewer changes in character, therefore having less appeal for discussion than the previous ones, the corresponding profiles are fewer as well. In general, the results indicate that a significant region of the flow is

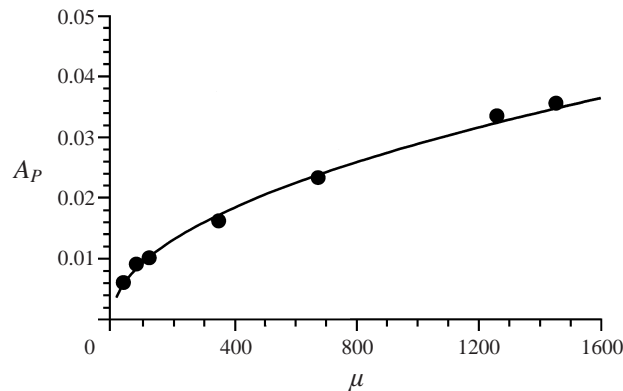


FIGURE 13. Measured pointwise amplitude of oscillations as a function of degree of criticality for $H/R = 3$.

approximately in solid-body rotation, especially in those profiles neighbouring (but not crossing) the rotor. The extent of this region is gradually reduced, as one moves away from the rotor, due to the action of viscous effects. The breakdown bubble also influences the circumferential velocity, though in a much more tenuous way than for the other components, as one might intuitively suspect. Its consequences are restricted to a moderate tendency to homogenize the swirling velocities in the flow area occupied by the recirculating bubble. This is in close agreement with the measurements of Bornstein & Escudier (1984), although a different geometry was under investigation. As general comment, measurements and predictions display an impressive consonance.

4.3. Unsteady breakdown

The experimental observations of vortex breakdown allowed us to conclude that the associated flow structures do not indefinitely maintain the steadiness exhibited by the regime studied in detail in the previous subsection. In fact, as depicted in figure 5 (dashed line), there is a critical value of the Reynolds number Re_C , for each value of the gap ratio H/R , beyond which the flow has a time-dependent behaviour. Inspection of the flow for moderate values of Re has indicated a character that was, apparently, perfectly periodic. From computational studies of swirling flow in a cylindrical container, Daube & Sørensen (1989), Lopez & Perry (1992) and Sørensen & Christensen (1995) have reported oscillatory vortex breakdown regimes of periodic or quasi-periodic nature. Both these simulations (though limited to axisymmetric formulations) and the present experiments suggest that a supercritical Hopf bifurcation may occur for such flows, as pointed out by Sørensen & Christensen (1995). This conjecture could be confirmed by the LDV measurements conducted in the study.

The low noise level in the LDV signals, when compared to the intensity of the periodic component (see power spectra in §4.4), made possible the measurement of the amplitude characterizing the oscillations. A gap ratio value of 3 was selected this time because, as already discussed, it produces flow regimes where two breakdown bubbles are seen to coexist, thus providing the expectation of more enticing flow dynamics when a periodic state is attained. Pointwise velocity measurements were then performed, for increasingly higher values of Re . The analysis was initiated when a dominant frequency was found in the power spectrum, as simple visual detection of

periodic motion has proved to be rather inaccurate owing to the reduced magnitude of initial oscillations. Figure 13 shows the normalized value of local amplitudes A_p as a function of the degree of criticality $\mu = (Re - Re_C)$. The measuring location was fixed at $(z/R, r/R) = (2.6, 0.6)$, near the stator, and mean amplitudes were calculated from velocity records containing 2^{13} samples. An accurate estimate for the value of Re_C , which indicates the onset of time-dependent behaviour, can be computed by performing a least-squares fit on $\ln(A_p) = a \ln(\mu) + b$ for best correlation. A correlation coefficient of 0.998 is obtained for $Re_C = 2435$, which appears to be reasonable, bearing in mind the fact that it was experimentally evaluated. The parameters in the above function are $a = 0.487$ and $b = -6.921$. Hence, the square-root dependence between A_p and μ , expressed by parameter a , constitutes irrefutable evidence of a regular Hopf bifurcation (see e.g. Lichtenberg & Lieberman 1992).

In his experiments on a cylindrical container, Escudier (1984) has observed that until a considerable penetration into the unsteady domain of the stability diagram, the flow shows negligible departure from axisymmetry. Conversely, Faler & Leibovich (1977) have stated that the phenomenon of vortex breakdown is intrinsically non-axisymmetric, though Leibovich (1984) has also considered the possibility of an exception for confined vortices at fairly low Reynolds numbers. In figure 4(*f*), which represents an instantaneous view of a time-dependent regime for $H/R = 3$ and $Re = 2970$, one may already perceive certain deviations from axisymmetry that are chiefly apparent in the structure of the secondary bubble. Other flow visualizations by Pereira & Sousa (1995), employing a rather intricate experimental procedure that involved digital processing of video images, have substantiated this observation, although without bringing additional insight into the underlying physical mechanisms. A clear and enlightening flow visualization for manifestly time-dependent regimes has been shown to be difficult to accomplish due to various factors, such as the three-dimensionality of the flow and the strong mixing occurring within the closed cylindrical container. This latter effect is further enhanced by a pulsatory behaviour, which precludes the successful use of a flow tracer. Irrespectively of these difficulties there seems to exist a consensus regarding the fact that, well inside the unsteady domain, vortex breakdown displays a non-axisymmetric character, which is corroborated by the assertions of all authors referred to above.

To provide additional information regarding the unsteady behaviour of the present flow, numerical simulations have been first carried out for a regime characterized by $H/R = 3$ and $Re = 2700$. This value of the Reynolds number translates into a relatively moderate value of the degree of criticality, i.e. $\mu = 265$. The full three-dimensional time-dependent Navier–Stokes equations have again been numerically solved, conforming to the discussion in the previous paragraph and the recommendations of Faler & Leibovich (1978). Limited by the available computing resources, the number of grid nodes used for the calculation of a steady regime in §4.2, i.e. 61 nodes in each of the three coordinate directions, could not be increased. The procedure for the definition of the initial condition was similar to that in the previous computation (though now $\Omega = 33.6 \text{ rad s}^{-1}$), except for the superimposition of a small non-axisymmetric perturbation to the initial velocity field in the axial direction. The flow was seen to undergo a prolonged transient characterized by irregularly oscillatory motion before attaining a purely periodic behaviour. A long simulation time (not shown) was required prior to obtaining the trace presented in figure 14. This is in agreement with the calculations of Tsitverblit (1993) for an axisymmetric cylindrical container: a non-dimensional simulation time $\nu t/R^2 = 1.5$ was requested to reach a state characterized by constant amplitude and frequency for $Re = 2765$ and

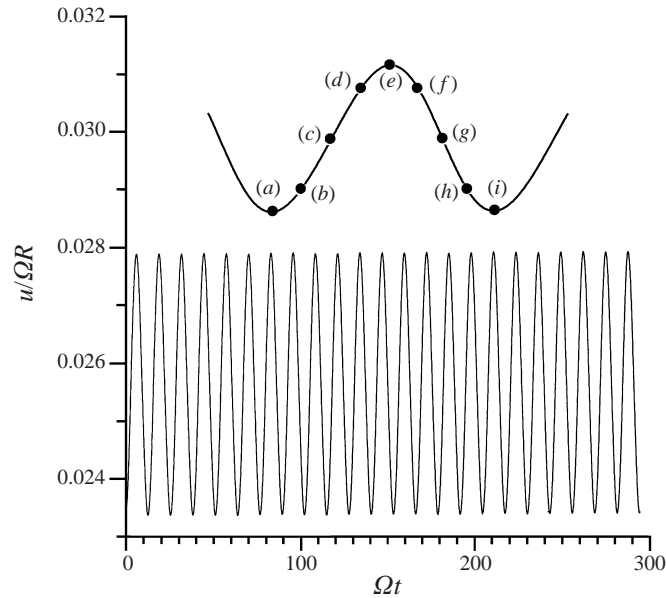


FIGURE 14. Oscillatory behaviour computed for $H/R = 3$ and $Re = 2700$ (the origin of the temporal axis is arbitrary).

$H/R = 2.5$, confirming the exceptionally high cost of the present three-dimensional computations. Figure 14 shows a purely periodic character of flow oscillations in the axial velocity component that is consistent with the experimentally observed Hopf bifurcation. The non-dimensional frequency extracted from the time-series was $\omega = 0.077$, favourably comparing with the experimental value $\omega = 0.075$ (see the next subsection for more details).

The dynamics of unsteady breakdown at $Re = 2700$ was numerically visualized by inserting passive particles in the flow. Best results were obtained by setting the circumferential flow to zero at this stage. The inclusion of the swirling velocity component has been shown to reduce the clarity of the resulting images, not allowing a proper examination of the innermost details of the flow. Figure 15(a–i) portrays, for this reason, instantaneous particle traces in a meridional plane, each image corresponding to a snapshot of the flow at the time instants marked in figure 14 by filled circles. Additionally, since the presence of a stagnation point in the central region of the flow has been defined as positive identification of vortex breakdown, surfaces of constant axial velocity $u = 0$ were represented in each image as well. However, the outer surface has been omitted for clarity. From the complete oscillation cycle depicted in figure 15, one immediately feels tempted to conclude that this regime is marked by a very close axisymmetry of the flow field. In fact, during the whole period of oscillation, neither the projection of outer structures in the meridional plane nor the surfaces circumscribing the three-dimensional region of reversed flow in the core display any significant deviation from symmetry. The topology of vortex breakdown bubbles at $Re = 2700$ seems very similar to that experimentally mapped in the previous subsection for $Re = 2570$, though the two vortex rings have clearly swollen with the increase in Re . Furthermore, these two structures exhibit appreciable quiescence, notwithstanding the nearly indiscernible ‘swinging’ expressed by the temporal evolution of instantaneous particles traces. In

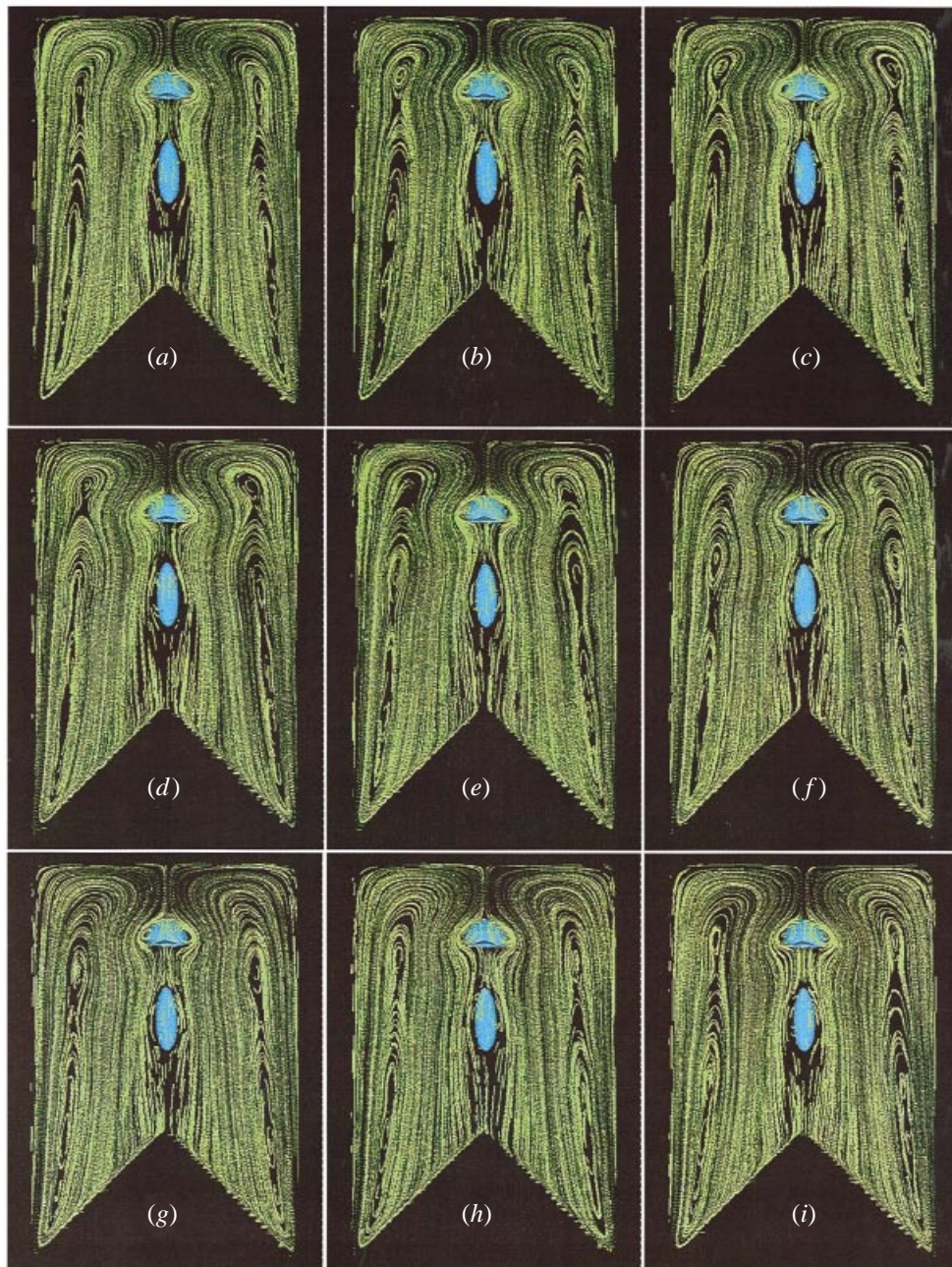


FIGURE 15. Planar-projected (instantaneous) particle traces at a meridional plane and surface of constant axial velocity ($u = 0$) in the core, for the time instants marked in figure 14.

contrast, all the region of the outer flow where the axial velocity changes sign shows intense activity. In the meridional plane, one may observe the signature of several vortical structures, actively partaking in the oscillatory process. The appearance of these cells, which were not found in steady regimes, is unquestionably linked to the establishment of unsteady flow.

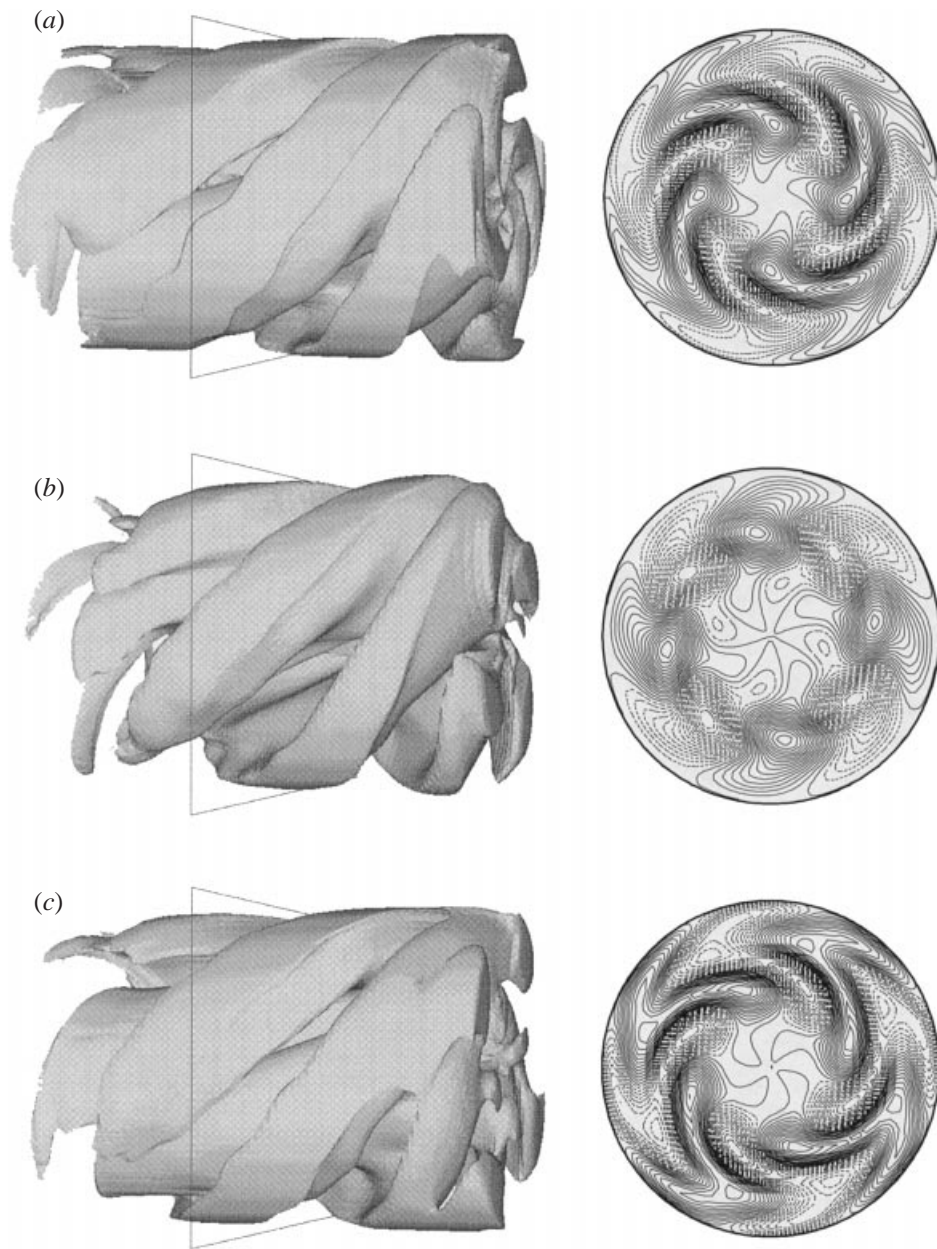


FIGURE 16. Disturbance mode that brings about the periodic oscillations, computed for $H/R = 3$ and $Re = 2700$ in terms of velocity components (three-dimensional surfaces of constant velocity and two-dimensional transverse cross-sections at $z/R = 1.5$): (a) axial (iso-surface value: 1×10^{-5} ; contour levels between -0.0020 and 0.0020); (b) radial (iso-surface value: 3×10^{-5} ; contour levels between -0.0015 and 0.0015); (c) circumferential (iso-surface value: 5×10^{-5} ; contour levels between -0.0015 and 0.0015). In all cases 31 levels were uniformly distributed between maximum and minimum values.

In order to proceed with a detailed analysis of the present regime, the disturbance mode responsible for the periodic behaviour of the flow has been calculated. Figure 16 portrays the result in terms of (a) axial, (b) radial and (c) circumferential components of the perturbation velocity. Both three-dimensional surfaces of constant velocity and two-dimensional transverse cuts at $z/R = 1.5$ are represented. Based on this figure, the reason why the flow regime may be misinterpreted as axisymmetric when viewing only meridional planes becomes readily obvious. The mode exhibits azimuthal periodicity of $\pi/2$ radians (wavenumber $n = 4$), resulting in the symmetry of the flow pattern with respect to the central axis for every meridional plane. However, if restricted to the vortex breakdown bubbles only, even a three-dimensional view of the structures may seem very closely axisymmetric. This may be explained by seeing that, in the vicinity of the central axis, the contours values of the velocity perturbations are constantly close to zero (see the cut planes in figure 16). It must also be mentioned that, with the course of time, the perturbation mode rotates. Bearing this in mind, a closer look to figure 16 brings additional insight about the flow dynamics. It can be seen that the surfaces of constant velocity perturbation have been shaped into four well-defined interpenetrating helices. The spinning motion of these ‘corkscrews’ clarifies the origin of the axial excursions of the cells observed in the meridional plane illustrated in figure 15. Thus, one may conclude that the vortical structures referred to in the previous paragraph actually consist of helical vortices. The origin of these vortices appears to be centrifugal instability, giving rise to the formation of vortex rings that are convected in spirals by the main flow and, ultimately, generating the unsteadiness. The observation that figure 16 shows the structures emanating from the region where centrifugal effects are large strongly supports the present conjecture. In agreement, in their investigation on the dynamics of confined vortices, Escudier *et al.* (1982) have attributed the formation of cells in the annular gap between the wall and the vortex core to centrifugal instability as well.

To discover whether the unsteady flow preserves the above-described planar symmetry, a second numerical simulation was carried out for higher the Re of 3100, increasing the degree of criticality to $\mu = 665$. The new value for the spinning velocity of the rotor was $\Omega = 38.6 \text{ rad s}^{-1}$. Other numerical parameters were, once again, kept unchanged. Following a very long simulation time ($vt/R^2 > 2$), the time trace shown in figure 17 was obtained. As expected, the (mean) amplitude of axial velocity oscillations has become larger, though exhibiting a certain irregularity from a low-frequency modulation. The dominant spectral component is characterized by a non-dimensional frequency $\omega = 0.079$. This value is in good agreement with the experimental measurement $\omega = 0.076$ (see the next subsection). The error of 4% in the determination of the frequency of oscillation may still be judged as lying within the boundaries of uncertainty for the experimental technique. However, the presence of a low-frequency component could not be detected in the experiments below $Re = 3900$; the only possible explanation is that, at early stages, very little energy is contained in this component.

The dynamics displayed by the oscillatory regime at $Re = 3100$ has been illustrated in the same way as figure 15: a new series of snapshots sampled at the time instants indicated in figure 17, is shown in figure 18(a–i). It is unquestionable that the flow breakdown is now notably non-axisymmetric. Moreover, the interaction among the various flow structures is significantly more complex. Apart from the fact that the two breakdowns still coexist during the whole oscillation process, one cannot call these structures quiescent anymore. First, though the surfaces encircling the regions of reversed flow in the core appear in figure 18(a–d) as a single entity, these can be seen

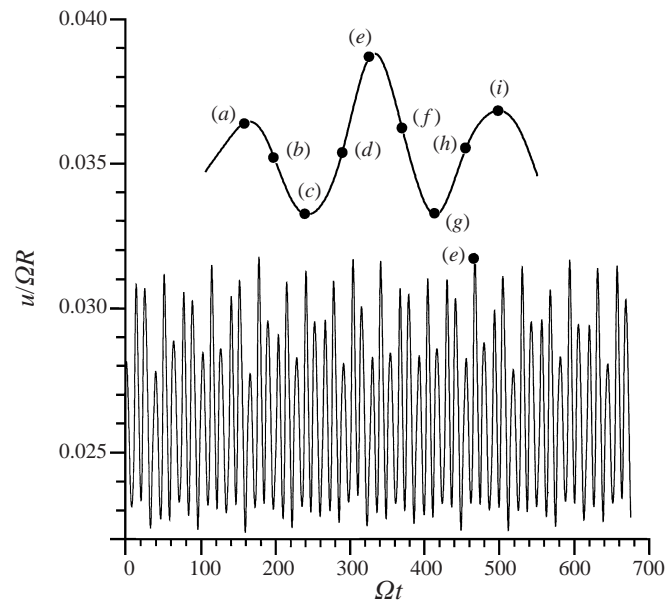


FIGURE 17. Oscillatory behaviour computed for $H/R = 3$ and $Re = 3100$ (the origin of the temporal axis is arbitrary).

detaching in figure 18(e) and merging again shortly after. This behaviour resembles that observed by Lopez (1990) in his simulations of a closed container for $H/R = 2.5$ and $Re = 2765$, who described the nature of the unsteadiness (paraphrasing) as: two bubbles coalescing and separating and coalescing etc. However, the dynamics of the breakdown structures depicted in figure 18 shows a clear three-dimensional character, which could never be found by Lopez due to the limitations imposed by an axisymmetric formulation. Secondly, the two breakdowns (separately or together) gyrate about the central axis in the same sense as the main flow. Although the surface associated with the primary breakdown maintains approximately the same shape as in the preceding flow regime, i.e. a semi-spherical cap, figure 18 demonstrates that this cap is now strongly tilted. As a consequence, the uppermost stagnation point describes a wide circular trajectory. On the other hand, the surface identified as the secondary breakdown has mutated into an S-shape (see e.g. figure 18f). In conjunction with the observation of the instantaneous trajectories shown by the passive tracer in figure 18, these facts attest that a shift from bubble- ($Re = 2700$) to spiral-type vortex breakdown ($Re = 3100$) has occurred. Further, the lack of any symmetry observed in the outer region reinforces this and strongly suggests that the flow became unstable to fully non-symmetric disturbances. Recent experimental investigations conducted by Brücker (1993) in a cylindrical channel, employing particle tracking velocimetry, have captured an instantaneous core flow topology exhibiting certain affinities with the one in the present simulations (see e.g. figures 18a and 18f). However, in the present case, the axial span of the spiral core is inhibited by the presence of the rotor.

The observations described in this section and the main findings reported by Escudier (1984) concur in essence: as here Escudier described two distinct regimes of unsteady breakdown, namely ‘steadily oscillating flow’ and ‘precession of the lower breakdown structure’. It is our conviction that the mechanisms governing the time-

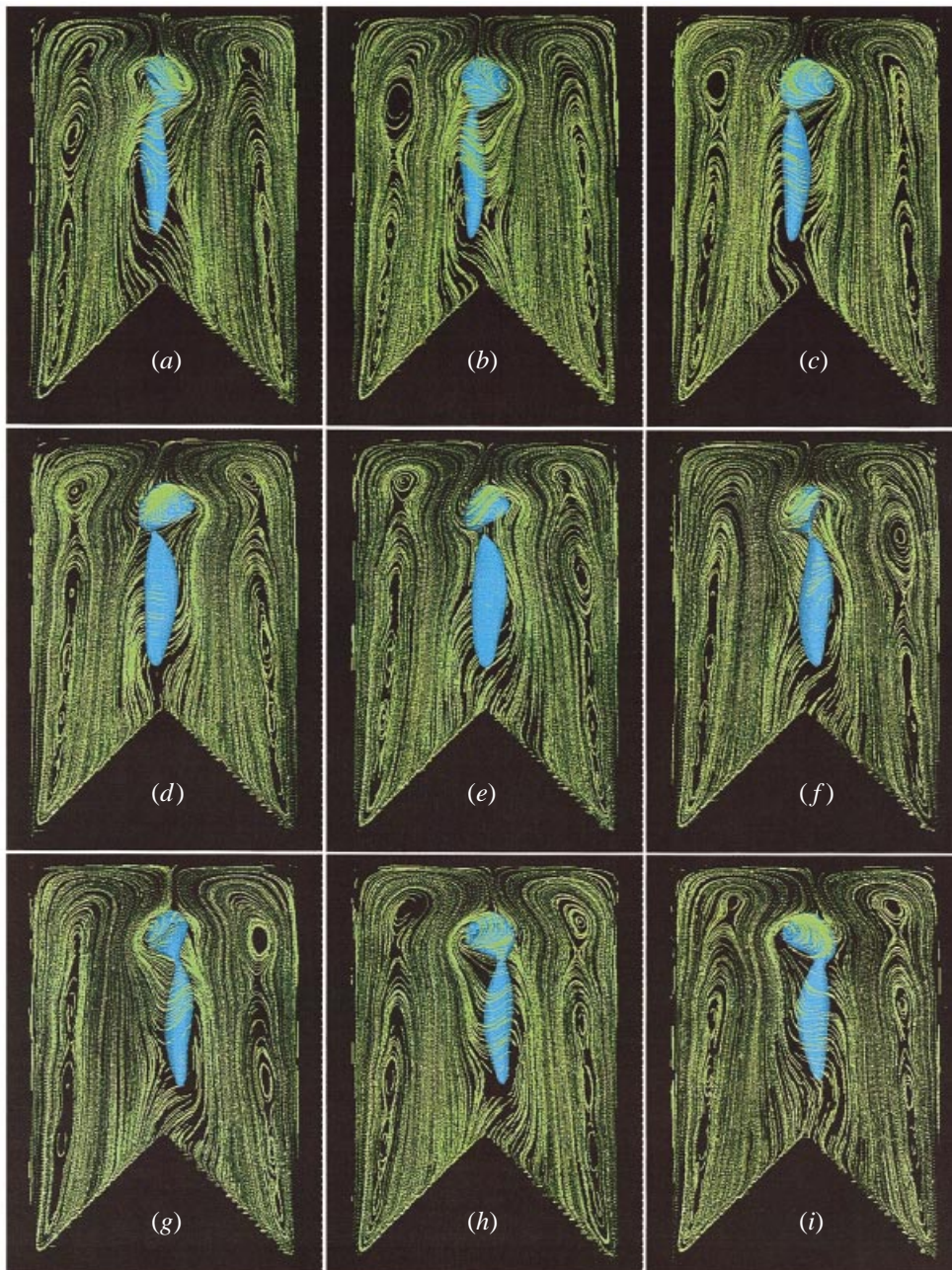


FIGURE 18. Planar-projected (instantaneous) particle traces at a meridional plane and surface of constant axial velocity ($u = 0$) in the core, for the time instants marked in figure 17.

dependent flow behaviour are qualitatively the same in both studies, despite the difference in the geometry of the rotor.

4.4. Transition to turbulence

In his experiments on a closed cylindrical container, Escudier (1984) observed that the continuing increase of the Reynolds number has the ultimate consequence of giving

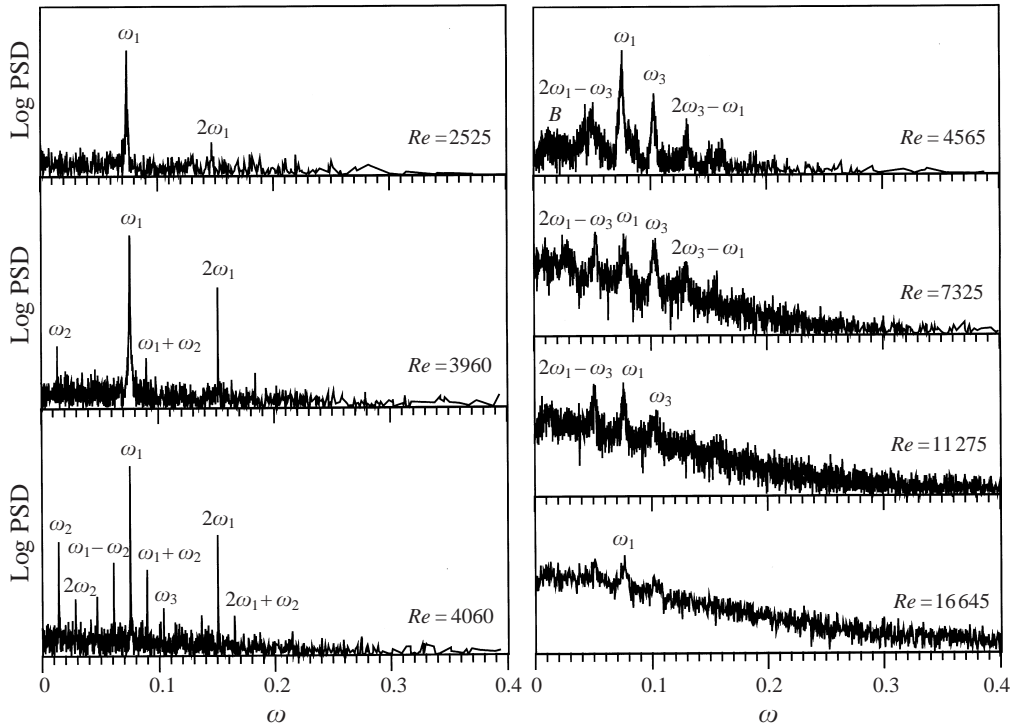


FIGURE 19. Measured u -velocity power spectra for $H/R = 3$ at various regimes.

rise to turbulent flow. The same observation was made for the confined swirling flow generated by a rotating cone described here. Thus, it is relevant to determine which physical mechanisms contributed to the route to turbulence exhibited by the present flow. However, the cost of the required numerical simulations is prohibitive, as we have concluded that such an investigation must reflect the markedly three-dimensional character of the flow at fairly high Re . For this reason, the study of the transition scenario was entirely experimental.

The investigations were based on the analysis of the spectral content of the flow, using LDV techniques to experimentally produce power spectra covering the various regimes up to turbulence. Special care was taken to ensure both stability of flow conditions and repeatability of results. Although without a significant outcome, the possible occurrence of hysteresis was also investigated. The majority of the present results concern observations for $H/R = 3$, as that was the value of the gap ratio selected for the study to determine the onset of unsteadiness. The case characterized by $H/R = 2$ is just briefly referenced, since it displayed similar features. However, it has shown less regularity in the repetition of the results.

The relevant u -velocity power spectra obtained from the experiments for $H/R = 3$ can be seen in figure 19, as a function of Re . The (logarithmic) power scale is arbitrary but it was kept unchanged throughout the measurements. Thus, figure 19 shows only a very slight increase in background noise level with the Reynolds number, up to $Re = 4565$. Beyond $Re = 7325$, however, the level of the background can be observed to increase monotonically. At a moderate value of Re , figure 19 indicates the establishment of a purely periodic state, characterized by a frequency ω_1 . In agreement with the analysis performed in §4.3, this regime appears at $Re =$

2435 as the result of a supercritical Hopf bifurcation. Subsequently, the periodic behaviour is substituted by a quasi-periodic state, described by the coexistence of two incommensurate frequencies, respectively ω_1 and ω_2 (plus linear combinations). Therefore, a second Hopf bifurcation occurs in the range $Re = 3865$ to $Re = 3960$. A new quasi-periodic state, characterized by three frequencies (ω_3 appears), is found at $Re = 4060$. During this process, the main components exhibit a continuous growth in power, ω_1 reaching a level nearly four orders of magnitude above that of the instrument noise background.

In the spectrum obtained at $Re = 4060$, some doubts arise whether the component identified as ω_3 , presumably associated with a third Hopf bifurcation, is really an independent frequency. In fact, the linear combination $2\omega_2 + \omega_1$ yields a value very close to that attributed to ω_3 . However, for $Re \geq 4565$ (see figure 19), the frequency component ω_3 is seen to persist while ω_2 definitely decreases. This observation seems to corroborate our view that a state with three incommensurate frequencies and no broadband noise was obtained at $Re = 4060$. In contrast, the disappearance of ω_2 at $Re = 4565$ is accompanied by the emergence of a weak component of broadband noise (labelled *B* in figure 19).

The sequence of events above, displaying a succession of Hopf bifurcations followed by a chaotic element, supports the conjecture that the Newhouse–Ruelle–Takens theorem applies to the present transition scenario (Ruelle & Takens 1971; Newhouse, Ruelle & Takens 1978). Our observations are in harmony with the predictions of these authors as the successive physical mechanisms can be classified as follows. First, the flow becomes unstable, approaching a stable periodic attractor (a limit cycle) topologically described by a one-dimensional torus T^1 in phase space. Secondly, the limit cycle becomes unstable and the new stable attractor yields a quasi-periodic flow on a torus T^2 , as the ratio ω_2/ω_1 has been shown to be irrational. A quasi-periodic regime on a three-dimensional torus T^3 follows, but this state is very sensitive to infinitesimal perturbations and transition to turbulence was seen to occur shortly after the detection of the third discrete frequency. Thus, the new attractor, usually referred as a ‘strange attractor’, takes over the flow, attracting trajectories in the phase space to a subspace where they perpetually wander in a chaotic pattern. The broad component associated with this behaviour arises in the area where ω_2 (that vanished) was formerly found, which makes this frequency a probable source of excitation. However, the combination $\omega_3 - \omega_1$ lies in the same frequency range as well, therefore *B* may well have been excited by the non linear interaction between modes ω_1 and ω_3 instead. In that case, the present mechanism would be strikingly similar to that observed by Fenstermacher, Swinney & Gollub (1979) for the transition to chaotic Taylor vortex flow.

The regime attained for $Re = 4565$ is only incipiently turbulent, still exhibiting a significant organization, which is expressed by the persistence of sharp peaks in the power spectrum. Further increasing Re , the evolution to complete turbulence continues. Following the initial strengthening of the periodic component ω_3 , a competition arises between ω_1 and $2\omega_3 - \omega_1$ for primacy over the flow, allied to the continuous increase of the continuum level. The maximum Reynolds number (using the present working fluid) was reached at $Re = 16\,645$ and the corresponding power spectrum displays most of the features characterizing a weakly turbulent flow. However, the frequency component ω_1 can still be identified, probably associated with the establishment of a turbulent flow with ‘precession of vortex core’ (PVC), which is known to be a frequent condition of highly swirling flows (Gupta, Lilley & Syred 1984).

Table 2 summarizes the transitions observed in confined swirling flow generated by

Reynolds number	Transition	Frequency components	Dynamical regime
2190	Vortex breakdown	None	Time-independent
2435	Hopf bifurcation	ω_1	Periodic
3865–3960	Hopf bifurcation	ω_1, ω_2	Quasi-periodic
3960–4060	Hopf bifurcation	$\omega_1, \omega_2, \omega_3$	Quasi-periodic
4345–4565	B appears	ω_1, ω_3, B	Weakly turbulent flow with several spectral components
~ 16645	ω_3 disappears	ω_1, B	Weakly turbulent flow with one spectral component

TABLE 2. Transitions in confined swirling flow generated by a rotating cone for $H/R = 3$.

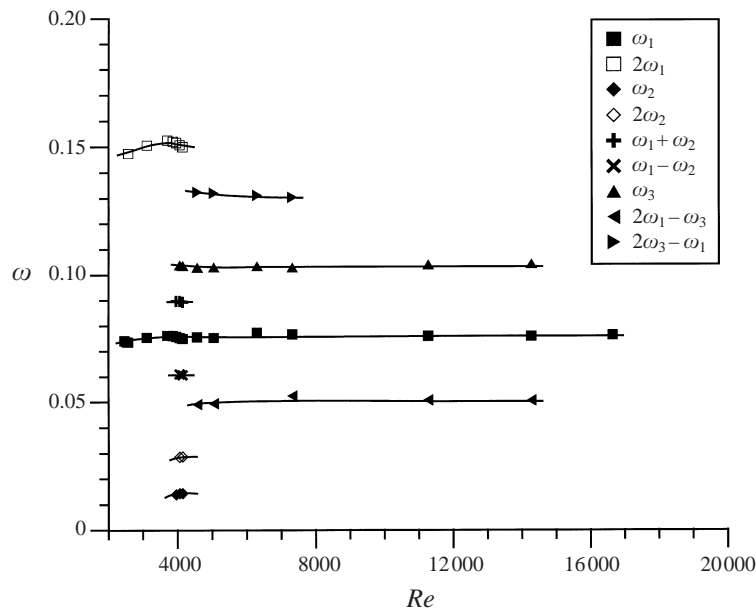


FIGURE 20. Measured non-dimensional frequencies of spectral components as a function of Reynolds number for $H/R = 3$.

a rotating cone for $H/R = 3$. Note that the present transition scenario is rather less intricate than that numerically established by Sørensen & Christensen (1995). The dissimilarities may be attributed to the differences in geometry, but it is our strong belief that these mainly result from the axisymmetric formulation adopted by the aforementioned authors, which we have shown to be physically unrealistic.

The experimentally determined frequency values have been shown to be approximately independent of Re , as depicted in figure 20. Nevertheless, ω_1 was seen to vary between 0.074 and 0.077 (smoothly increasing), while ω_2 and ω_3 assumed the values 0.014 and 0.103, respectively. Such a small dependence of the dominant frequency ω_1 on the Reynolds number is somewhat surprising, since it is well known that the period of a Hopf bifurcation is amplitude dependent. As shown in figure 13 (see § 4.3), the amplitude of the oscillation grows with the square root of the degree of criticality. However, the measured oscillation amplitudes were relatively small throughout. This

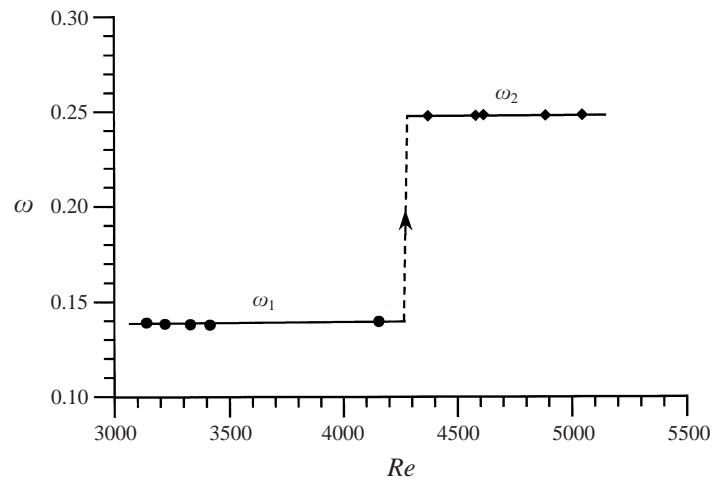


FIGURE 21. 'Frequency jump' observed for $H/R = 2$.

fact was also confirmed by the numerical simulations carried out for $Re = 2700$ and 3100 (see figures 14 and 17).

As mentioned earlier, the investigation of the case characterized by $H/R = 2$ indicated a transition picture that was essentially similar to the one described for $H/R = 3$. At values of Re below 3095, it was not possible to find any periodic components in the flow. However, in the range defined by $Re = 3095$ and $Re = 4885$, the flow exhibited a purely periodic behaviour. At $Re = 5045$ two frequencies were simultaneously measured, respectively $\omega_2 = 0.248$ and $\omega_3 = 0.013$, characterizing a quasi-periodic flow. The most salient feature observed for $H/R = 2$ was the 'frequency jump' shown in figure 21. A discontinuity in the evolution of the non-dimensional frequency is seen occurring between $Re = 4155$ and $Re = 4370$, promoting a jump from $\omega_1 = 0.138$ to $\omega_2 = 0.248$ (both regimes were periodic). The change in the frequency of oscillation might be due to a reorganization of the flow structures inside the cylindrical container that was not visualized. This would explain why the phenomenon could not be found for a larger value of the gap ratio, i.e. $H/R = 3$, as a larger volume is available for the flow structures in this case. It is curious to note that, once again, there was a parallel in the results of Fenstermacher *et al.* (1979).

5. Concluding remarks

The swirling flow driven by a rotating cone within a closed cylindrical container has been under investigation. The experimental study embraced flow visualization and laser-Doppler velocity measurements of the entire flow field. Three-dimensional time-dependent numerical simulations have been carried out as well. A semi-implicit (Crank-Nicholson/Adams-Bashforth) method was used for the time advancement and a second-order central finite difference scheme was employed in the discretization of spatial derivatives.

Experiments and numerical simulations have demonstrated that, for some combinations of Reynolds number and gap ratio, bubble-type vortex breakdown occurs. The topology of steady breakdown has been shown to be similar to that reported by Escudier (1984), corresponding to ring-like structures. As a consequence, many similarities could also be found when establishing a stability diagram for the present

flow. Numerical simulations have been compared with detailed velocity measurements at Reynolds number 2200, for a gap ratio of 2. The extent of the agreement between these two techniques has been carefully examined and was found to be very good.

Once again in accordance with the work of Escudier (1984), oscillatory flow regimes were detected when the Reynolds number exceeded a critical value, which varied with the gap ratio. The experimentally observed periodic behaviour indicated that the mechanism responsible for transition to unsteady flow was a supercritical Hopf bifurcation. Numerical simulations of two time-dependent regimes characterized by $Re = 2700$ and 3100 for $H/R = 3$ have revealed the dynamics of breakdown structures. At $Re = 2700$, it was seen that the initially axisymmetric steady flow sustained the growth of a three-dimensional disturbance of azimuthal wavenumber $n = 4$, giving rise to a stable time-periodic regime. Nevertheless, the breakdowns exhibited negligible departure from axisymmetry at this stage and retained the original topology, i.e. the two vortex rings. In contrast, primary and secondary breakdowns were seen merging and separating during the oscillation process at $Re = 3100$. Furthermore, these structures were observed in precession about the central axis, portraying a fully non-symmetric behaviour. Such a dramatic change in the nature of the oscillatory motion was attributed to a shift from bubble- ($Re = 2700$) to spiral-type breakdown ($Re = 3100$). Altogether, these facts sanction the idea, also recently put forward by other researchers, that three-dimensional time-dependent simulations of the phenomenon must be performed to achieve full understanding of the underlying physics.

From an examination of velocity power spectra measured throughout the unsteady flow regimes, a route to turbulence could be deduced. Repeated bifurcations yielded transitions to periodic and quasi-periodic flows, respectively characterized by one, two and three discrete frequencies (and, eventually, higher harmonics). The appearance of a third frequency was followed by the onset of broadband noise and chaotic motion. Thus, on increasing the Reynolds number, a weakly turbulent regime was reached. At the maximum value of the parameter attained in the experiments, the corresponding power spectrum still exhibited one spectral component, which was presumably due to precession of the vortex core.

Finally, the authors have strong reasons to believe that, similarly to what was unequivocally verified for steady breakdown, the physical mechanisms governing the unsteady breakdown regimes disclosed in the present study are qualitatively the same as in the flows investigated by Escudier (1984).

The computing facilities provided by 'Fundação para a Computação Científica Nacional' for the accomplishment of numerical simulations are gratefully acknowledged.

REFERENCES

- ADRIAN, R. J. 1983 Laser velocimetry. In *Fluid Mechanics Measurements* (ed. R. J. Goldstein). Hemisphere.
- ADRIAN, R. J. & YAO, C. S. 1987 Power spectra of fluid velocities measured by laser Doppler velocimetry. *Exps. Fluids* **5**, 17.
- BENDAT, J. S. & PIERSOL, A. G. 1971 *Random Data: Analysis and Measurement Procedures*. Wiley Interscience.
- BENJAMIN, T. B. 1962 Theory of the vortex breakdown phenomenon. *J. Fluid Mech.* **14**, 593.
- BENJAMIN, T. B. 1967 Some developments in the theory of vortex breakdown. *J. Fluid Mech.* **28**, 65.
- BORNSTEIN, J. & ESCUDIER, M. P. 1984 LDA measurements within a vortex-breakdown bubble. In

- Laser Anemometry in Fluid Mechanics* (ed. R. J. Adrian, D. F. G. Durão, F. Durst, H. Mishina & J. H. Whitelaw). Ladoan – Instituto Superior Técnico.
- BREUER, M. & HÄNEL, D. 1983 A dual time-stepping method for 3-D, viscous, incompressible vortex flows. *Comput. Fluids* **22**, 467.
- BROWN, G. L. & LOPEZ, J. M. 1990 Axisymmetric vortex breakdown. Part 2. Physical mechanisms. *J. Fluid Mech.* **221**, 553.
- BRÜCKER, C. 1993 Study of vortex breakdown by particle tracking velocimetry (PTV). Part 2: Spiral-type vortex breakdown. *Exps. Fluids* **14**, 133.
- BRÜCKER, C. & ALTHAUS, W. 1992 Study of vortex breakdown by particle tracking velocimetry (PTV). Part 1: Bubble-type vortex breakdown. *Exps. Fluids* **13**, 339.
- BRÜCKER, C. & ALTHAUS, W. 1995 Study of vortex breakdown by particle tracking velocimetry (PTV). Part 3: Time-dependent structure and development of breakdown-modes. *Exps. Fluids* **18**, 174.
- CASSIDY, J. J. & FALVEY, H. T. 1970 Observations of unsteady flow arising after vortex breakdown. *J. Fluid Mech.* **41**, 727.
- COELHO, P. & PEREIRA, J. C. F. 1993 Calculation procedure for 3-D laminar flows in complex geometries using a nonstaggered nonorthogonal grid system. *Appl. Math. Modelling* **17**, 562.
- DAUBE, O. & SØRENSEN, J. N. 1989 Simulation numérique de l'écoulement périodique axisymétrique dans une cavité cylindrique. *C. R. Acad. Sci. Paris* **308**, 463.
- DIMOTAKIS, P. E. 1976 Single scattering particle laser Doppler measurements of turbulence. In *Applications of Non-Intrusive Instrumentation in Flow Research*. Saint-Louis.
- DURST, F., MELLING, A. & WHITELAW, J. H. 1981 *Principles and practice of Laser-Doppler Anemometry*. Academic.
- EDWARDS, R. V. & JENSEN, A. S. 1983 Particle -sampling statistics in laser anemometers: Sample-and-hold systems and saturable systems. *J. Fluid Mech.* **133**, 397.
- ERDMANN, J. C., LEHMANN, B. & TROPEA, C. 1986 The statistical bias of laser anemometry applied in sinusoidal flowfields. In *Laser Anemometry in Fluid Mechanics – II* (ed. R. J. Adrian, D. F. G. Durão, F. Durst, H. Mishina & J. H. Whitelaw). Ladoan – Instituto Superior Técnico.
- ESCUDIER, M. P. 1983 Vortex breakdown in the absence of an endwall boundary layer. *Exps. Fluids* **1**, 193.
- ESCUDIER, M. P. 1984 Observations of the flow produced in a cylindrical container by a rotating endwall. *Exps. Fluids* **2**, 189.
- ESCUDIER, M. 1987 Confined vortices in flow machinery. *Ann. Rev. Fluid Mech.* **19**, 27.
- ESCUDIER, M. 1988 Vortex breakdown: observations and explanations. *Prog. Aerospace Sci.* **25**, 189.
- ESCUDIER, M. P., BORNSTEIN, J. & MAXWORTHY, T. 1982 The dynamics of confined vortices. *Proc. R. Soc. Lond. A* **382**, 335.
- ESCUDIER, M. P., BORNSTEIN, J. & ZEHNDER, N. 1980 Observations and LDA measurements of confined turbulent vortex flow. *J. Fluid Mech.* **98**, 49.
- ESCUDIER, M. P. & KELLER, J. J. 1983 Vortex breakdown: a two-stage transition. *AGARD CP-342*.
- ESCUDIER, M. P. & KELLER, J. J. 1985 Recirculation in swirling flow: a manifestation of vortex breakdown. *AIAA J.* **23**, 111.
- ESCUDIER, M. P. & ZEHNDER, N. 1982 Vortex-flow regimes. *J. Fluid Mech.* **115**, 105.
- FALER, J. H. & LEIBOVICH, S. 1977 Disrupted states of vortex flow and vortex breakdown. *Phys. Fluids* **20**, 1385.
- FALER, J. H. & LEIBOVICH, S. 1978 An experimental map of the internal structure of a vortex breakdown. *J. Fluid Mech.* **86**, 313.
- FENSTERMACHER, P. R., SWINNEY, H. L. & GOLLUB, J. P. 1979 Dynamical instabilities and transition to chaotic Taylor vortex flow. *J. Fluid Mech.* **94**, 103.
- GARG, A. K. & LEIBOVICH, S. 1979 Spectral characteristics of vortex breakdown flowfields. *Phys. Fluids* **22**, 2053.
- GUPTA, A. K., LILLEY, D. G. & SYRED, N. 1984 *Swirl Flows*. Abacus.
- HALL, M. G. 1972 Vortex breakdown. *Ann. Rev. Fluid Mech.* **4**, 195.
- HARVEY, J. K. 1962 Some observations of the vortex breakdown phenomenon. *J. Fluid Mech.* **14**, 585.
- JONES, J. P. 1960 The breakdown of vortices in separated flow. *University of Southampton, USAA Rep.* 140.

- KOBAYASHI, M. H. & PEREIRA, J. C. F. 1991 Numerical comparison of momentum interpolation methods and pressure-velocity algorithms using non-staggered grids. *Commun. Appl. Numer. Meth.* **7**, 173.
- LAMBOURNE, N. C. & BRYER, D. W. 1961 The bursting of leading-edge vortices—some observations and discussion of the phenomenon. *Aero. Res. Council. R. & M.* 3282.
- LAWLEY, T. J. & PRICE, D. C. 1972 Design of vortex fluid amplifiers with asymmetrical flow fields. *Trans. ASME: J. Dyn. Syst. Meas. Control* **94**, 82.
- LEIBOVICH, S. 1978 The structure of vortex breakdown. *Ann. Rev. Fluid Mech.* **10**, 221.
- LEIBOVICH, S. 1984 Vortex stability and breakdown: survey and extension. *AIAA J.* **22**, 1192.
- LEIBOVICH, S. & KRIBUS, A. 1990 Large-amplitude wavetrains and solitary waves in vortices. *J. Fluid Mech.* **216**, 459.
- LEIBOVICH, S. & STEWARTSON, K. 1983 A sufficient condition for the instability of columnar vortices. *J. Fluid Mech.* **126**, 335.
- LESSEN, M., SINGH, P. J. & PAILLET, F. 1974 The stability of a trailing line vortex. Part 1. Inviscid theory. *J. Fluid Mech.* **63**, 753.
- LICHTENBERG, A. J. & LIEBERMAN, M. A. 1992 *Regular and Chaotic Dynamics*. Springer.
- LIU, C. H. & MENNE, S. 1989 Numerical investigation of a three-dimensional vortex breakdown. *Fourth Asian Congress of Fluid Mechanics, Hong Kong*.
- LOPEZ, J. M. 1990 Axisymmetric vortex breakdown. Part 1. Confined swirling flow. *J. Fluid Mech.* **221**, 533.
- LOPEZ, J. M. & PERRY, A. D. 1992 Axisymmetric vortex breakdown. Part 3. Onset of periodic flow and chaotic advection. *J. Fluid Mech.* **234**, 449.
- LUGT, H. J. & ABOUD, M. 1987 Axisymmetric vortex breakdown with and without temperature effects in a container with a rotating lid. *J. Fluid Mech.* **179**, 179.
- LUGT, H. J. & HAUSSLING, H. J. 1982 Axisymmetric vortex breakdown in rotating fluid within a container. *Trans. ASME: J. Appl. Mech.* **49**, 921.
- MERZKIRCH, W. 1974 *Flow Visualization*. Academic.
- NEWHOUSE, S., RUELLE, D. & TAKENS, F. 1978 Occurrence of strange Axiom A attractors near quasi-periodic flows on $T^m, m \geq 3$. *Commun. Math. Phys.* **64**, 35.
- PECKHAM, D. H. & ATKINSON, S. A. 1957 Preliminary results of low speed wind tunnel tests on a Gothic wing of aspect ratio 1.0. *Aero. Res. Council. CP-508*.
- PEREIRA, J. C. F. 1989 Refractive index matching for LDV measurements near walls and in complex geometries. In *Instrumentation for Combustion and Flow in Engines* (ed. D. F. G. Durão, J. H. Whitelaw & P. O. Witze). Kluwer.
- PEREIRA, J. C. F. & SOUSA, J. M. M. 1993 Finite volume calculations of self-sustained oscillations in a grooved channel. *J. Comput. Phys.* **106**, 19.
- PEREIRA, J. C. F. & SOUSA, J. M. M. 1995 Flow visualization study on sealed large-gap-ratio rotor-stator systems. In *Flow Visualization VII* (ed. J. Crowder). Begell House.
- RANDALL, J. D. & LEIBOVICH, S. 1973 The critical state: a trapped wave model of vortex breakdown. *J. Fluid Mech.* **58**, 495.
- RHIE, C. M. & CHOW, W. L. 1983 Numerical study of turbulent flow past an airfoil with trailing edge separation. *AIAA J.* **21**, 1525.
- ROACHE, P. J. 1976 *Computational Fluid Dynamics*. Hermosa.
- RONNENBERG, B. 1977 Ein selbstjustierendes 3-Komponenten-Laserdoppleranemometer nach dem vergleichsstrahlverfahren, angewandt für Untersuchungen in einer stationären zylindersymmetrischen Drehströmung mit einem Rückstromgebiet. *Max-Planck-Inst. Bericht* 20.
- RUELLE, D. & TAKENS, F. 1971 On the nature of turbulence. *Commun. Math. Phys.* **20**, 167.
- SARPKAYA, T. 1971a On stationary and travelling vortex breakdowns. *J. Fluid Mech.* **45**, 545.
- SARPKAYA, T. 1971b Vortex breakdown in swirling conical flows. *AIAA J.* **9**, 1792.
- SARPKAYA, T. 1974 Effect of the adverse pressure gradient on vortex breakdown. *AIAA J.* **12**, 602.
- SØRENSEN, J. N. & CHRISTENSEN, E. A. 1995 Direct numerical simulation of rotating fluid flow in a closed cylinder. *Phys. Fluids* **7**, 764.
- SOUSA, J. M. M. 1995 Experimental and numerical investigation of fluid flow instability and transition. Doctoral thesis, Instituto Superior Técnico, Technical University of Lisbon (in Portuguese).

- SPALL, R. E., GATSKI, T. B. & ASH, R. L. 1990 The structure and dynamics of bubble-type vortex breakdown. *Proc. R. Soc. Lond. A* **429**, 613.
- SQUIRE, H. B. 1960 Analysis of the 'vortex breakdown' phenomenon. Part I. *Imperial College, Aero. Dept. Rep.* 102.
- STONE, H. L. 1968 Iterative solutions of implicit approximations of multidimensional partial differential equations. *SIAM J. Numer. Anal.* **5**, 530.
- SYRED, N. & BEÉR, J. M. 1974 Combustion in swirling flows. *Combust. Flame* **23**, 143.
- THOMPSON, J. F., WARSI, Z. U. A. & MASTIN, C. W. 1985 *Numerical Grid Generation—Foundations and Applications*. North-Holland.
- TSITVERBLIT, N. 1993 Vortex breakdown in a cylindrical container in the light of continuation of a steady solution. *Fluid Dyn. Res.* **11**, 19.
- VOGEL, H. U. 1968 Experimentelle Ergebnisse über die laminare Strömung in einen zylindrischen Gehäuse mit darin rotierender Scheibe. *Max-Planck-Inst. Bericht* 6.
- YANTA, W. J. & SMITH, R. A. 1973 Measurements of turbulence-transport properties with a laser Doppler velocimeter. *AIAA 11th Aerospace Science Meeting, Washington*.